

Tilted black hole accretion disc models of Sagittarius A*: time-variable millimetre to near-infrared emission

Jason Dexter^{1*} and P. Chris Fragile²

¹Theoretical Astrophysics Center and Department of Astronomy, University of California, Berkeley, CA 94720-3411, USA

²Department of Physics & Astronomy, College of Charleston, Charleston, SC 29424, USA

10 November 2018

ABSTRACT

High-resolution, multi-wavelength, and time-domain observations of the Galactic centre black hole candidate, Sgr A*, allow for a direct test of contemporary accretion theory. To date, all models have assumed alignment between the accretion disc and black hole angular momentum axes, but this is unjustified for geometrically thick accretion flows like that onto Sgr A*. Instead, we calculate images and spectra from a set of numerical simulations of accretion flows misaligned (“tilted”) by 15° from the black hole spin axis and compare them with millimetre (mm) to near-infrared (NIR) observations. Non-axisymmetric standing shocks from eccentric fluid orbits dominate the emission, leading to a wide range of possible image morphologies. These effects invalidate previous parameter estimates from model fitting, including estimates of the dimensionless black hole spin, except possibly for very low values of spin or tilt (upper limits of $a < 0.3$ or $\beta < 15^\circ$). At 1.3mm, the black hole images still have crescent morphologies, and the black hole shadow may still be accessible to future very long baseline interferometry (mm-VLBI) observations. Shock heating leads to multiple populations of electrons, some at high energies ($T_e > 10^{12}\text{K}$). These electrons can naturally produce the observed NIR flux, spectral index, and rapid variability (“flaring”). This NIR emission is uncorrelated with that in the mm, which also agrees with observations.

These are the first models to self-consistently explain the time-variable mm to NIR emission of Sgr A*. Predictions of the model include significant structural changes observable with mm-VLBI on both the dynamical (hour) and Lense-Thirring precession (day-year) timescales; and $\simeq 30 - 50\mu\text{s}$ changes in centroid position from extreme gravitational lensing events during NIR flares, detectable with the future VLT instrument GRAVITY. We further predict that multi-wavelength monitoring should find no significant correlations between mm and NIR/X-ray light curves. The weak correlations reported to date are shown to be consistent with our model, where they are artifacts of the short light curve durations. If the observed NIR emission is caused by shock heating in a tilted accretion disc, then the Galactic centre black hole has a positive, non-zero spin parameter ($a > 0$).

Key words: accretion, accretion discs — black hole physics — radiative transfer — relativity — galaxy: centre

1 INTRODUCTION

Due to its proximity, Sgr A* is the most intensively studied supermassive black hole candidate and the largest in angular size. Recent very long baseline interferometry observations at 1.3mm (mm-VLBI Doeleman et al. 2008; Fish et al. 2011) have detected source structure on event-horizon scales (tens of microarcseconds, μas). Future measurements with this Event Horizon Telescope may detect the black hole shadow, providing the first direct evidence for an event horizon (Bardeen 1973; Falcke, Melia & Agol 2000; Dexter et al. 2010).

The spectral energy distribution of Sgr A* rises from the radio to a peak in the submillimetre (mm “bump”). The radio emission is synchrotron radiation from non-thermal electrons far from the black hole, either in the accretion flow (Yuan, Quataert & Narayan 2003) or in a mildly relativistic jet (Falcke & Markoff 2000). The mm bump is well described by synchrotron radiation from hot ($\sim 10^{10-11}\text{K}$), mostly thermal electrons in the immediate vicinity of the black hole ($r \simeq 5 - 10M^1$ Yuan, Quataert & Narayan 2003; Mościbrodzka et al. 2009; Dexter et al. 2010).

In addition to 30 – 50 per cent variability in the mm

* E-mail: jdexter@berkeley.edu

¹ We frequently use units with $G = c = 1$; in these units for Sgr A* 1M is approximately $6 \times 10^{11}\text{cm}$ and 20s.

(Zhao et al. 2003; Yusef-Zadeh et al. 2006; Eckart et al. 2006; Marrone et al. 2008), Sgr A* is observed to “flare” rapidly in the NIR (Genzel et al. 2003; Ghez et al. 2004) and the X-ray (Baganoff et al. 2001) with order of magnitude amplitudes. The NIR/X-ray flares occur simultaneously (Eckart et al. 2004), and weak correlations in simultaneous light curves have suggested possible lags between NIR/X-ray and mm variability (Yusef-Zadeh et al. 2008). The NIR (X-ray) emission is either synchrotron radiation from energetic electrons, or inverse Compton scattering of mm (NIR) seed photons (Markoff et al. 2001).

No theoretical model of Sgr A* self-consistently accounts for the observed time-variable multi-wavelength emission. Radiatively inefficient accretion flow (RIAF Yuan, Quataert & Narayan 2003) and jet (Falcke & Markoff 2000) models can describe the multi-wavelength “quiescent” spectrum. RIAF models also provide excellent fits to existing mm-VLBI data (Broderick et al. 2009, 2011).

Models for the NIR flares include coherently orbiting inhomogeneities (“hotspots” Broderick & Loeb 2006) in the inner radii of the accretion flow. Recently, correlated multiwavelength flares have instead favored an adiabatically expanding blob model (Yusef-Zadeh et al. 2009; Eckart et al. 2012), which can explain the reported time lags between the NIR/X-ray and mm flares. The blobs could be formed from non-thermal events such as magnetic reconnection in the accretion flow (Dodds-Eden et al. 2010).

All of these models are non-relativistic. They neglect the magnetic fields responsible for angular momentum transport and accretion via the magnetorotational instability (MRI, Balbus & Hawley 1991). Magnetohydrodynamic (MHD) simulations can provide a more physical description of the accretion flow. They have been used to model the synchrotron emission from Sgr A*, either in three spatial dimensions with a pseudo-Newtonian potential (Ohsuga, Kato & Mineshige 2005; Goldston, Quataert & Igumenshchev 2005; Huang et al. 2009; Chan et al. 2009), or in full general relativity (GRMHD) in two (Noble et al. 2007; Mościbrodzka et al. 2009) or three (Dexter, Agol & Fragile 2009; Dexter et al. 2010; Shcherbakov, Penna & McKinney 2010; Dolence et al. 2012) dimensions. Non-relativistic simulations are especially inappropriate for modeling the mm/NIR/X-ray emission, which originates in the innermost portion of the accretion flow where relativistic effects are strongest. Axisymmetric simulations cannot sustain the MRI, and cannot accurately model variability.

Existing models from 3D simulations provide an excellent description of mm observations including polarization (Shcherbakov, Penna & McKinney 2010), variability and mm-VLBI (Dexter, Agol & Fragile 2009; Dexter et al. 2010). These models also produce large amplitude NIR flares (Dolence et al. 2012), but with much lower fluxes and steeper spectral indices than observed. Although current global GRMHD simulations are factors of a few in resolution from convergence (Hawley, Guan & Krolik 2011), the resulting spectra of Sgr A* are fairly insensitive to resolution (Shiokawa et al. 2012).

There are two major limitations to current models. First, the electron distribution function is highly uncertain. Most theoretical models adopt a thermal distribution for the mm bump, and some add a non-thermal power law tail. Models from simulations use a thermal distribution with a constant electron-ion temperature ratio, T_i/T_e , allowing the electron temperature to be calculated from the output density and pressure (Goldston, Quataert & Igumenshchev 2005; Mościbrodzka et al. 2009). Simple prescriptions for allowing this ratio to vary spatially lead to only minor changes in the images/spectra. This parameter can be calibrated either using phys-

ically motivated sub-grid models for electron heating (Sharma et al. 2007) or through direct particle-in-cell calculations of MRI turbulence (Riquelme et al. 2012). The second major limitation to all existing theoretical models of Sgr A*, and the subject of this article, is the assumption that the accretion flow angular momentum axis is aligned with the black hole spin axis.

Geometrically thick accretion flows like that onto Sgr A* do not align with a central black hole as geometrically thin discs do (Bardeen & Petterson 1975). Sgr A* is currently fed by the winds of young, massive stars (Quataert 2004), whose net angular momentum axis is not expected to be aligned with the spin axis of Sgr A*. The only way for alignment to occur is then for the black hole to accrete an amount of material with constant angular momentum orientation comparable to its mass. For this to occur in a Hubble time requires an accretion rate $\sim 10^{-4} \dot{M}_{\text{yr}^{-1}}$, an order of magnitude larger than the estimated accretion rate at the Bondi radius (Yuan, Quataert & Narayan 2003) and several orders of magnitude larger than that onto Sgr A* ($10^{-7} - 10^{-9} M_{\odot} \text{yr}^{-1}$ Aitken et al. 2000; Bower et al. 2003; Marrone et al. 2007). Therefore, it is highly likely that the accretion flow is misaligned (“tilted”).

The expected disc misalignment has extraordinary consequences for the dynamics and observable properties of a black hole accretion flow. Lense-Thirring precession leads to tilts and warps that are oscillatory functions of radius (Ivanov & Illarionov 1997), and gravitational torques cause the entire disc to precess essentially as a solid body (Fragile et al. 2007). Eccentric orbits in the disc converge, leading to non-axisymmetric standing shocks (Fragile & Blaes 2008). Excess angular momentum transport from the shocks truncates the accretion flow outside of the marginally stable orbit (Fragile 2009; Dexter & Fragile 2011). The asymmetry of the accretion flow leads to images and spectra that depend strongly on the observer azimuthal viewing angle (Dexter & Fragile 2011).

In this work we calculate time-dependent images and spectra from the only published GRMHD simulations of tilted black hole accretion discs (Fragile et al. 2007, 2009; Fragile 2009), and compare them with mm to NIR observations of Sgr A*. We review the physics of tilted accretion discs in §2 and describe the numerical simulations in §3. The methods used to construct radiative models from the simulations are outlined in §4. These radiative models are then fit to existing mm-VLBI and spectral observations in §5, and the mm images and mm to NIR spectral and variable properties of the best-fitting models are analyzed in §6. The implications and limitations of this study are discussed in §7, and the major results are summarized in §8.

2 TILTED BLACK HOLE ACCRETION DISCS

Whenever a black hole accretion disc is tilted, it experiences differential Lense-Thirring precession owing to the frame dragging of the rotating black hole. In a disc, Lense-Thirring precession is able to build up over many orbital periods, so it can affect the structure well beyond radii normally associated with relativistic effects.

The effect of Lense-Thirring precession in a disc is to cause it to warp, and this warping can propagate through the disc in either a diffusive or wave-like manner. In the diffusive case, the warping is limited by “viscous” responses within the disc, and the Lense-Thirring precession dominates out to a unique transition radius r_{BP} (Bardeen & Petterson 1975; Kumar & Pringle 1985), inside of which the disc is expected to be flat and aligned with the black-hole midplane, and outside of which it is also expected to be flat but in

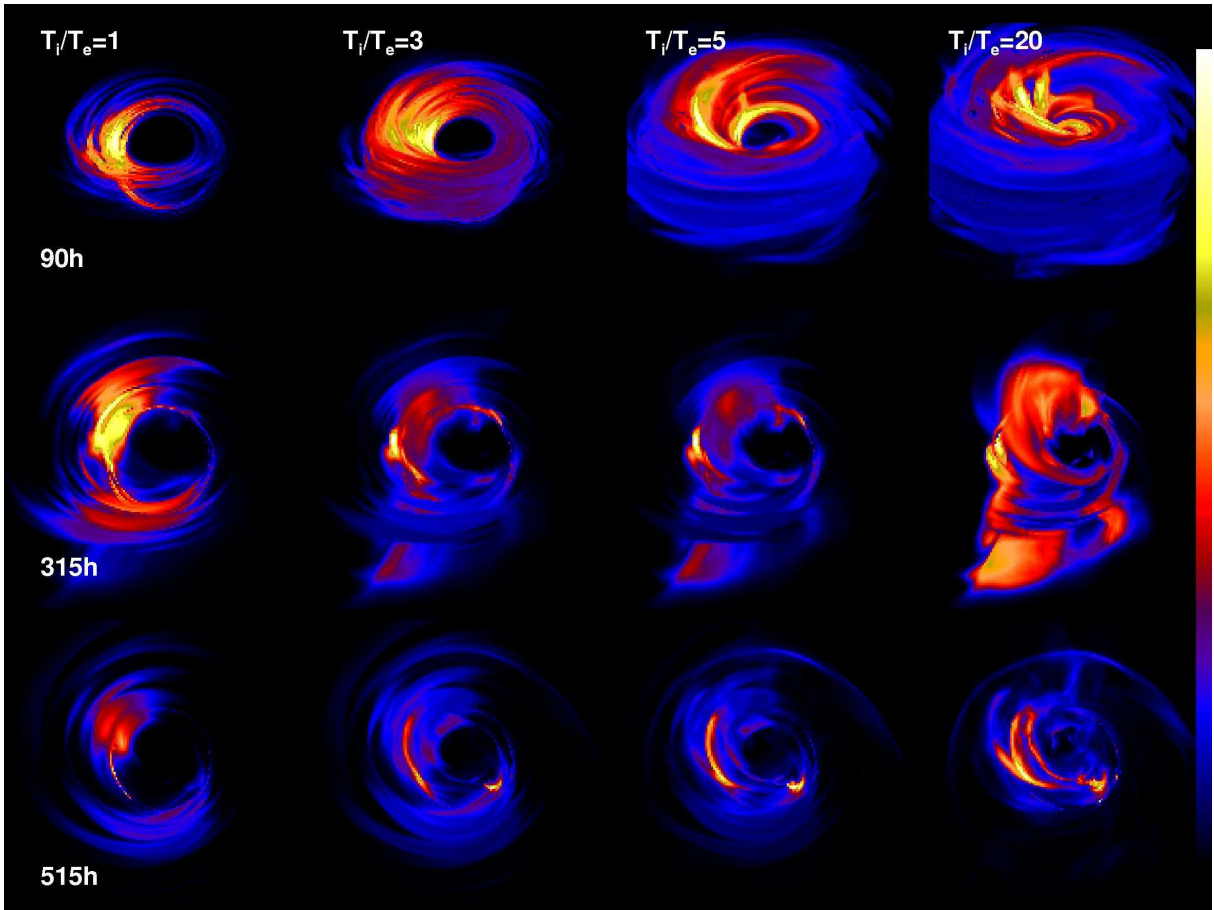


Figure 1. Images as a function of T_i/T_e for the 90h, 315h, and 515h simulations. The colours are scaled linearly with a dynamic range of 60, and the images are $160 \times 160 \mu\text{as}$ in all cases. Images from untilted simulations such as 90h become optically thick and emit from a growing photosphere with increasing T_i/T_e . Images from tilted simulations do not become uniformly optically thick, and can even become smaller at large T_i/T_e , as in the case of 515h, due to the presence of multiple electron populations with varying electron temperatures at distinct spatial locations in the accretion flow.

a plane determined by the angular momentum of the gas reservoir. This “Bardeen-Petterson” configuration is expected for Keplerian discs whenever the dimensionless stress parameter α is larger than the ratio H/r , where H is the disc semi-thickness. Given that α is usually considered to be significantly less than one, this requires geometrically thin discs.

In thicker discs, such as would be expected in low-luminosity sources such as Sgr A*, warps propagate in a wave-like manner, and the disc does not go into the Bardeen-Petterson configuration. Instead, the tilt of the disc can be an oscillatory function of radius, with the amplitude of the oscillations growing as one approaches the black hole (Ivanov & Illarionov 1997). These oscillations are stationary, however, so they cannot act to absorb the torque of the black hole. For thick discs, this torque instead causes the disc to precess as if it were a solid body.

The warping of tilted thick discs creates unbalanced pressure gradients that can drive significant latitude-dependent epicyclic motion within the disc. The induced motion of the gas can be coherent over the entire scale of the disc, with magnitudes that are substantial fractions of the orbital velocity. Radial variations in the eccentricity of the associated fluid-element trajectories can lead to a crowding of orbit trajectories at certain locations within the disc. This results in local density enhancements akin to compressions. These compressions can be sufficiently strong to produce standing

Table 1. Simulation Parameters

Simulation	a	β	Reference
315h	0.3	15°	Fragile (2009)
515h	0.5	15°	Fragile et al. (2009)
715h	0.7	15°	Fragile (2009)
90h	0.9	0°	Fragile et al. (2007)
915h	0.9	15°	Fragile et al. (2007)

shocks within the disc, particularly in the vicinity of the black hole (Fragile & Blaes 2008).

Tilted accretion disc models can be constructed semi-analytically using height-integrated equations in the so-called twisted frame (Ivanov & Illarionov 1997; Zhuravlev & Ivanov 2011). However, these models lack the magnetic fields that lead to angular momentum transport in the disc and give rise to the observed synchrotron emission from Sgr A*. They also have an unconstrained vertical structure, leading to additional free parameters. Finally, they are stationary, and so cannot be used to study variability self-consistently. Instead, we employ 3D GRMHD simulations of misaligned black hole accretion discs. Simulations have fewer free parameters and higher physical fidelity. Few exist, however, preventing anything like a thorough exploration of the parameter space in dimensionless black hole spin, disc tilt, and geometric disc thickness.

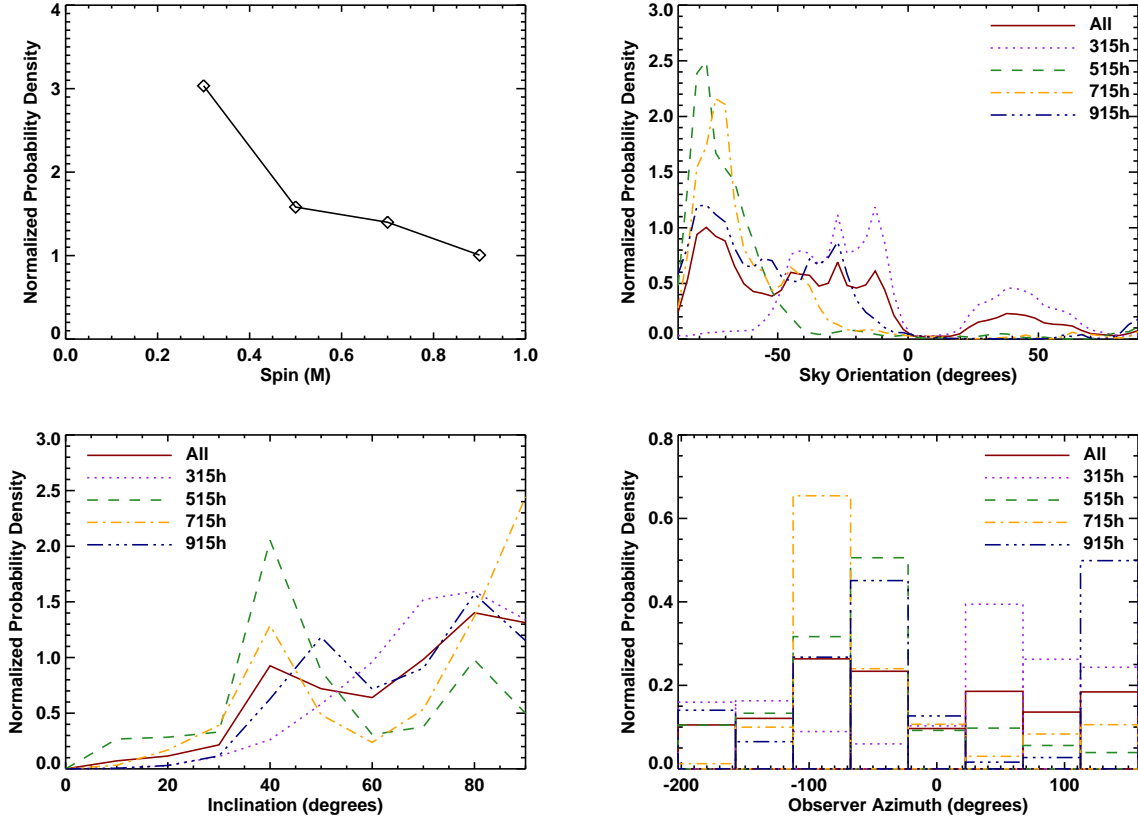


Figure 2. Normalized probability distributions as functions of black hole spin (top left), observer inclination (top right), sky orientation (bottom left), and observer azimuth (bottom right) for each simulation separately and combined (solid lines). Unlike in aligned models (Broderick et al. 2009, 2011; Dexter et al. 2010) the parameters of the viewing geometry are essentially unconstrained.

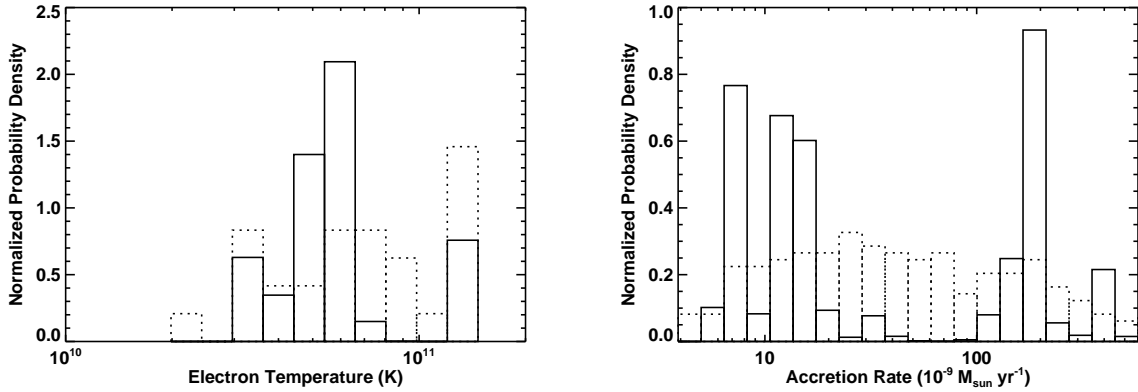


Figure 3. Normalized probability density as a function of electron temperature (left) and accretion rate (right), marginalized over the other parameters. The electron temperature is taken to be the median in the region of largest emissivity for each model. The accretion rate is time-averaged for each model. In both cases, probability densities for models falling in each bin are added to make the histogram. The dotted histograms in both panels are the result of assigning equal probability to each model. The viable range of accretion rates is much larger than in aligned simulations (Dexter, Agol & Fragile 2009; Dexter et al. 2010), while the electron temperature remains well constrained to a narrow region around the observed brightness temperature.

3 SIMULATIONS

The numerical data used in our analysis were taken from simulations presented in Fragile et al. (2007), Fragile et al. (2009), and Fragile (2009). All of the simulations used the Cosmos++ GRMHD code (Anninos, Fragile & Salmonson 2005). Cosmos++ includes

several schemes for solving the GRMHD equations; in these simulations, the internal-energy, artificial viscosity formulation was used. The magnetic fields were evolved in an advection-split form, while using a hyperbolic divergence cleanser to maintain an approximately divergence-free magnetic field. The GRMHD equations were evolved in a “tilted” Kerr-Schild polar coordinate system

$(t, r, \vartheta, \varphi)$. This coordinate system is related to the usual (untilted) Kerr-Schild coordinates (t, r, θ, ϕ) through a simple rotation about the y -axis by an angle β , as described in Fragile & Anninos (2005).

The simulations were carried out on a spherical polar mesh with nested resolution layers. The base grid contained 32^3 mesh zones and covered the full 4π steradians. Two levels of refinement were added on top of the base layer; each refinement level doubling the resolution relative to the previous layer, thus achieving peak resolutions equivalent to a 128^3 simulation. In the radial direction a logarithmic coordinate of the form $\eta \equiv 1.0 + \ln(r/r_{\text{BH}})$ was used, where r_{BH} is the black-hole horizon radius. In the angular direction, in addition to the nested grids, a concentrated latitude coordinate x_2 of the form $\vartheta = x_2 + \frac{1}{2}(1-h)\sin(2x_2)$ was used with $h = 0.5$ to concentrate resolution toward the midplane of the disc.

The simulations started from the analytic solution for an axisymmetric torus around a rotating black hole (Chakrabarti 1985). The inner radius of the torus was $r_{\text{in}} = 15M$; the radius of the initial pressure maximum was $r_{\text{centre}} = 25M$; and the power-law exponent used in defining the initial specific angular momentum distribution was $q = 1.68$. An adiabatic equation of state was assumed, with $\Gamma = 5/3$. The torus was seeded with a weak dipole magnetic field in the form of poloidal loops along the isobaric contours within the torus. The field was normalized such that initially $\beta_{\text{mag}} = P/P_B \geq \beta_{\text{mag},0} = 10$ throughout the torus. The black hole was inclined by an angle $\beta = 0^\circ$ or 15° relative to the disc (and the grid). From this starting point, the simulations were allowed to evolve for a time equivalent to 10 orbits at the initial pressure maximum, r_{centre} , corresponding to hundreds of orbits at the ISCO. Table 1 summarizes the simulation parameters.

4 RADIATIVE MODELING

A radiative model is specified by three components: a dynamical model for fluid variables as functions of space and time; a model for the electron distribution function; and an emission model. In this work, the GRMHD simulations described above are used as the dynamical model. As in previous radiative models of Sgr A* from simulations (Goldston, Quataert & Igumenshev 2005; Mościbrodzka et al. 2009; Dexter et al. 2010), we employ a thermal Maxwell-Jüttner distribution for the electrons, assuming a constant ion-electron temperature ratio, T_i/T_e , as a crude approximation to the electron distribution function in a collisionless plasma. This ratio is a free parameter in the models. Finally, we assume the emission is entirely from synchrotron radiation, and use the unpolarized emission coefficient from Leung, Gammie & Noble (2011).

With these assumptions, observables can be calculated from the simulations using ray tracing. Starting from an observer's camera, rays are traced backwards in time toward the black hole (assuming they are null geodesics) using the public code GEOKERR (Dexter & Agol 2009). In the region where rays intersect the accretion flow, the radiative transfer equation is solved along the geodesic using the code GRTRANS (Dexter 2011), which then represents a pixel of the image. This procedure is repeated for many rays to produce an image, and at many time steps of the simulation to produce time-dependent images (movies). Light curves are computed by integrating over the individual images. Repeating the procedure over observed wavelengths gives a time-dependent spectrum.

To calculate fluid properties at each point on a ray, the space-time coordinates of the geodesic are transformed from Boyer-

Lindquist to the tilted Kerr-Schild coordinates used in the simulations. Since the accretion flow is dynamic, light travel time delays along the geodesic are taken into account. Data from the sixteen nearest zone centres (eight on the simulation grid over two time steps) were interpolated to each point on the geodesic. The simulations are scale free, and must be scaled to cgs units in order to calculate emission and absorption coefficients. Fixing the black hole mass ($M_{\text{bh}} \simeq 4 \times 10^6 M_\odot$ for Sgr A*) sets the length and timescales. The total mass in the accretion flow is a free parameter, and its choice is equivalent to fixing the time-averaged accretion rate. To convert image intensities to flux, we adopt a distance $D = 8\text{kpc}$ to the Galactic centre.

For each simulation, images are produced over a grid of parameters at 0.4mm and 1.3mm: dimensionless black hole spin, a (or equivalently simulation); time-averaged accretion rate, \dot{M} ; ion-electron temperature ratio, T_i/T_e ; observer inclination, i , azimuth, ϕ_0 , and sky orientation (position angle measured E of N), ξ . These images (including the effects of interstellar scattering, Bower et al. 2006) are fit jointly to mm-VLBI observations (Doeleman et al. 2008; Fish et al. 2011) and spectral measurements (Marrone 2006). This gives the probability of observing the measured values from a particular model, which is converted to the probability distribution as a function of the model parameters using the method described in Broderick et al. (2009) and used in Dexter et al. (2010). This procedure gives a joint probability distribution as a function of the above parameters. To estimate individual parameters, we marginalize over the others using uniform priors on a , T_i/T_e , ϕ_0 , and ξ ; a logarithmic prior on \dot{M} , and a $\sin i$ prior on the inclination angle.

In practice, the range of \dot{M} is used to bracket the range of observed mm (230 GHz) fluxes from Sgr A*: $\approx 2 - 5\text{Jy}$. Achieving convergence requires a fine enough grid so that multiple images have mm fluxes close to those observed by mm-VLBI ($\simeq 2.4\text{Jy}$) and spectral observations ($\simeq 3.5 - 4.25\text{Jy}$). In untilted simulations, this is possible with a fairly coarse grid of 10 \dot{M} values, since the image structure is nearly unchanged as the flux varies by 30 – 50 per cent (see §6.1). Variability then acts to sample the total flux more finely. This is not the case in tilted simulations, where the image structure changes drastically on short timescales. In probability distributions over both observer time and position angle (ξ), reasonable convergence is obtained when using 20 values of \dot{M} .

The observer azimuth, ϕ_0 , is a new parameter for tilted simulations, since the accretion flow is no longer azimuthally symmetric on times much longer than the orbital time. Instead, non-axisymmetric structure in these simulations averages out only on the much longer precession timescale.² Also unlike untilted simulations, the non-axisymmetric structure dominates images from tilted discs (Dexter & Fragile 2011). We find that 8 values of ϕ_0 are sufficient to capture the range of model images.

4.1 Sgr A* millimetre emission region

The mm emission in Sgr A* is at the peak of the SED and the transition from optically thick to thin, and is primarily produced by thermal electrons. The emission comes from a photosphere where the optical depth $\tau \simeq 1$, so that the temperature of the emitting electrons is given by the brightness temperature, T_b :

² The simulations considered here have durations of $\approx t_{\text{prec}}/8$.

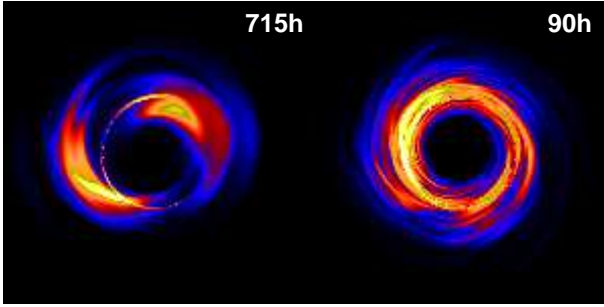


Figure 4. Nearly face-on images from the 715h (left) and 90h (right) simulations scaled as in Figure 1. The structure in images from untilted simulations such as 90h is mostly azimuthally symmetric (circularly symmetric when viewed face-on), while that in the tilted simulations such as 715h is highly non-axisymmetric due to the presence of standing shocks which dominate the mm emission in models of Sgr A*. In addition, asymmetries in untilted images travel at the orbital speed, whereas the standing shocks travel at the much slower Lense-Thirring precession speed.

$$kT_b = \frac{c^2 I_{\nu_0}}{2\nu_0^2} \simeq 6 \times 10^{10} \left(\frac{F_{\nu_0}}{3 \text{ Jy}} \right) \left(\frac{\nu_0}{230 \text{ GHz}} \right)^{-2} \left(\frac{\Delta\theta}{40 \mu\text{as}} \right)^{-2} \text{ K}, \quad (1)$$

where F_{ν_0} (I_{ν_0}) is the observed flux (specific intensity) at frequency ν_0 , and $\Delta\theta$ is the observed linear angular size of the emitting region scaled to the value found recently from mm-VLBI observations (Doeleman et al. 2008; Fish et al. 2011). This is effectively a lower limit for the models, since in the tilted disc models the accretion flow can be completely optically thin at 1.3mm. However, the electron temperatures in these cases are still within a factor of 2 of T_b . This is why even for a wide range of simulations, T_i/T_e , and \dot{M} , the electron temperature is well constrained for both the untilted (Dexter et al. 2010) and tilted (§5) models.

In untilted simulations, the accretion flow effectively consists of one population of electrons – those in the inner radii near the midplane, where temperatures, field strengths, and particle densities are highest. The best-fitting value of T_i/T_e in untilted simulations is then that for which this electron population has $T_e \simeq T_b$. At higher values of T_i/T_e , a larger accretion rate is required to match the observed flux ($j_\nu \propto M^2 T_e^2 / M^3$). The absorption coefficient is less strongly dependent on T_e than the emission coefficient ($\alpha_\nu \propto j_\nu / B_\nu \propto j_\nu / T_e$ in LTE), so that absorption becomes increasingly important for higher T_i/T_e . The accretion flow then develops a photosphere which grows outwards in radius with increasing T_i/T_e . This effect is shown in the top row of Figure 1 for the 90h simulation. Other untilted simulations behave similarly, except that in conservative simulations (e.g., MBD or MBQ in Dexter et al. 2010, from McKinney & Blandford 2009) the T_i values are larger and hence so are the favored values of T_i/T_e .

The brightness temperature argument holds for the tilted simulations as well (see §5). However, heating from the standing shocks effectively leads to additional electron populations at varying densities, field strengths, and ion temperatures, depending on latitude. The densest material with the lowest ion temperature is near the (tilted) midplane, and is brightest for small T_i/T_e . The densities and field strengths decrease away from the midplane, and these populations of electrons become more important at higher T_i/T_e . The material closer to the midplane becomes optically thick as T_i/T_e increases, but not nearly as much as in untilted simulations.

This is because the emissivity of hotter electrons also increases, and these electrons are largely unobscured by optically thick material.

Changing T_i/T_e then can either lead to a growing photosphere, or it can simply increase the emissivity of electrons that previously had $T_e > T_b$, causing structural changes without the image necessarily becoming optically thick. This effect can lead to a complicated dependence of the image on T_i/T_e , as shown in the bottom two rows of Figure 1 for the 315h and 515h simulations. While the 315h image becomes increasingly optically thick with increasing T_i/T_e , it does so much more slowly than the untilted simulations. The 515h simulation begins to grow a photosphere until hotter electrons dominate the image at $T_i/T_e \gtrsim 3$, after which the photosphere begins to recede. These images remain qualitatively similar from $T_i/T_e \approx 20 - 200$.

5 SGR A* PARAMETER CONSTRAINTS

Even with the limited coverage and sensitivity of current mm-VLBI data, it is possible to estimate parameters of both the black hole and accretion flow in Sgr A* in the context of either RIAF (Broderick et al. 2009, 2011) or GRMHD models (Dexter et al. 2010; Dexter 2011). The inclination and position angles are particularly well constrained, and are in excellent agreement between the two types of models. Both models assume alignment between the disc and black hole, which is almost certainly not the case for Sgr A*.

For the tilted disc simulations with a misalignment of 15° , there are many possible models which provide excellent fits to current mm observations (reduced χ^2 from a single epoch of mm-VLBI of $\lesssim 0.6$). The wide range of images is mostly due to the strong changes with observer time and azimuth, both of which have minimal effects on the structure of untilted disc images. As a result, the parameters of the model are essentially unconstrained with current observations (Figures 2 and 3). We can formally estimate the parameter values as: $i = 80^\circ_{-42^\circ}^{+10^\circ}$, $\xi = -78^\circ_{-11^\circ}^{+130^\circ}$, $\dot{M} = 165_{-161}^{+284} \times 10^{-9} M_\odot \text{yr}^{-1}$, and $T_e = 4_{-1}^{+7} \times 10^{10} \text{K}$, all to 90 per cent confidence. All values of ϕ_0 are allowed at this confidence. More data and a more complete set of simulations will be required to meaningfully constrain the parameters. All previous models have assumed a disc tilt of zero, and have found much stronger constraints on Sgr A* parameters than we find for a tilt of 15° . Previously reported parameter estimates are then invalid except for either very low values of tilt or spin ($a < 0.3$ or $\beta < 15^\circ$ are the upper limits from these simulations).

As in untilted models, face-on inclinations are disfavored, primarily because they are too optically thin to explain the observed spectral indices (Mościbrodzka et al. 2009). A wide range of position angles are viable, but the location of the broad peak in probability density corresponds to the range found for untilted models (Dexter et al. 2010; Broderick et al. 2011). In each model, an observer azimuth is favored where velocities downstream of one of the non-axisymmetric shocks are approaching the observer. For 915h, both such orientations are favored, while in the other simulations the probability distribution is asymmetric with one standing shock favored.

As discussed above (§4), it is non-trivial to find all viable values of T_i/T_e for the tilted simulations. Since a higher accretion rate is required at higher T_i/T_e to match the observed flux of Sgr A*, this leads to a wide range of possible accretion rates, unlike the untilted case. However, the electron temperature is still well constrained. Lowering T_i/T_e and increasing the accretion rate serves

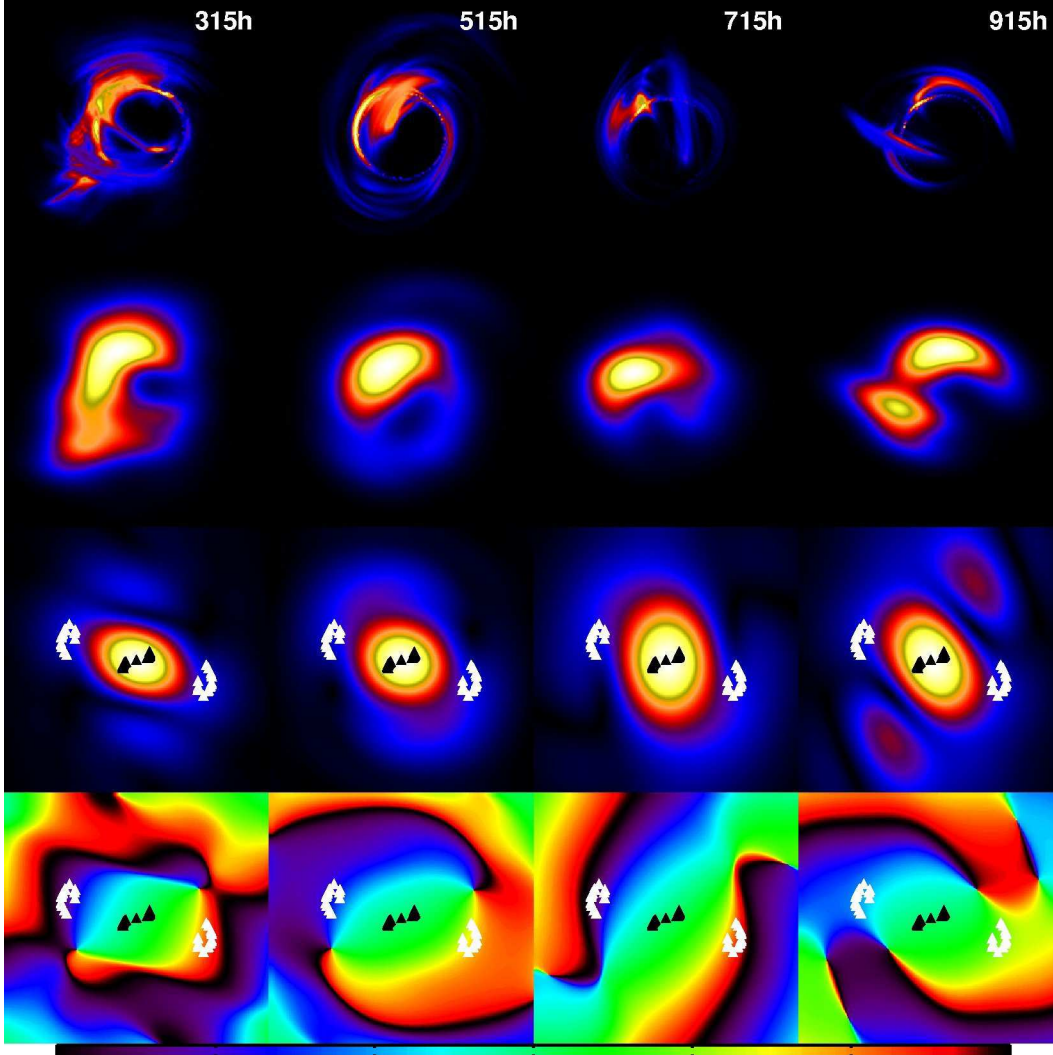


Figure 5. Best-fitting images from each simulation (columns) with (second row) and without (top row) the effects of interstellar scattering, as well as the corresponding visibility amplitudes (third row) and phases (fourth row) for $\nu_0 = 1.3\text{mm}$ (230 GHz). Image scales are the same as in Figure 1. The visibility amplitudes also have a dynamic range of 60, and both the visibility amplitude and phase images are $1200 \times 1200 M\lambda$ in size. The phase colours range from blue (negative) to green (zero) to red (positive). The triangles show the locations of existing mm-VLBI observations. Once convolved with interstellar scattering, the best-fitting images are crescents with significant but non-dominant Doppler beaming. The black hole shadow appears as a local minimum in the visibility amplitude, and a region of rapidly varying phase.

Table 2. Best Fit Model Parameters

Name	Spin	$\dot{M} (10^{-9} M_{\odot} \text{yr}^{-1})$	i	ξ	ϕ_0	T_i/T_e
315h	0.3	130	70°	-13°	$\pi/4$	3
515h	0.5	18	40°	-81°	$-\pi/4$	1
715h	0.7	10	90°	-70°	$-\pi/2$	1
915h	0.9	6	80°	-38°	$3\pi/4$	1

to pick out different electrons, but does not change their temperature by more than a factor of two.

6 MODEL PROPERTIES

Despite the lack of robust or meaningful parameter constraints, there are many generic properties of the images, spectra, and light curves of tilted accretion disc models with important observational implications for Sgr A*. The best-fitting models from each simulation are representative of the range of viable possibilities from our

fitting, and in this section these models are studied in detail. Their parameters are given in Table 2.

6.1 Images

The importance of non-axisymmetric standing shocks for Sgr A* images is shown in Figure 4. Images from a tilted simulation (715h, left panel) are dominated by material heated by the standing shocks, which appear as non-axisymmetric, roughly $m = 2$ structures. Any non-axisymmetric structure in untilted images (right panel of Figure 4) travels at the orbital speed, while the standing shocks move at the much slower precession speed. In addition to the choice of T_i/T_e described above, images from tilted simulations are then primarily set by observer azimuth, which determines the viewing orientation of the standing shocks.

The asymmetry of the tilted disc images leads to a wide range of complex image morphologies, which depending on the model

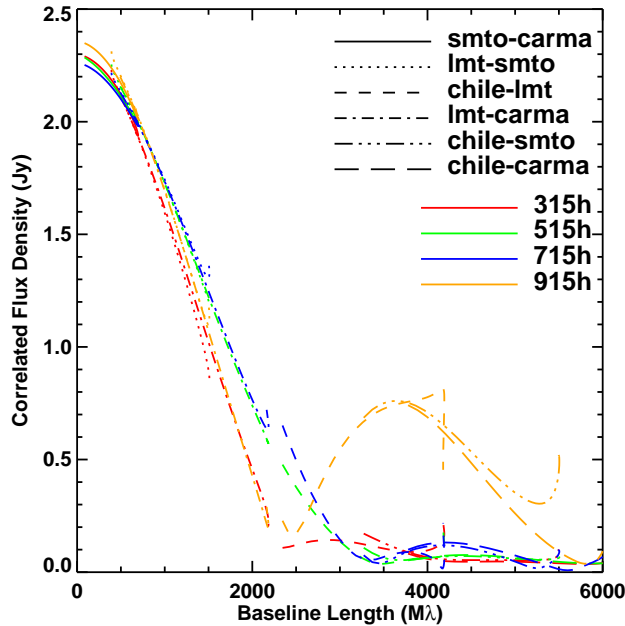


Figure 6. Visibility amplitude vs. baseline length for the best-fitting models interpolated to the uv locations of current and future baselines. The local minimum in the visibility amplitudes for 515h and 715h near $3000M\lambda$ is a signature of the black hole shadow.

and observer time can be dominated either by the post-shock fluid, dense material near the midplane of the tilted disc, or other hot electrons. This is the primary reason that the model parameters cannot be well constrained thus far. Despite the additional complexity, viable images tend to be similar. This is demonstrated using the best-fitting models from all simulations, whose 1.3mm images (top row of Figure 5) are all “crescents,” as found previously for images from untilted simulations (Dexter et al. 2010). The crescent morphology results from a combination of strong Doppler beaming from orbital disc motion, which causes asymmetry between approaching and receding material, and gravitational lensing, which causes the back of the accretion flow to appear above and below the black hole in the image. The crescent morphology is especially apparent when the images are convolved with interstellar scattering (second row of Figure 5), which at 1.3mm blurs most of the small scale image structure. The black hole shadow is apparent as a central minimum in all images, at the orientation corresponding to light coming from the back of the accretion flow, which is bent above and below the black hole. The shadow appears in the visibility amplitude (third row of Figure 5) as a local minimum on the same orientation at a baseline whose length corresponds to the size scale of the shadow in the image. It also appears at the same location as a region of rapidly varying visibility phase (fourth row of Figure 5).

We can make predictions for future mm-VLBI observations by interpolating visibilities to the locations of future baselines between ALMA/APEX in Chile, LMT in Mexico, and current telescopes: SMTO in Arizona, JCMT/SMA in Hawaii, and CARMA in California. The results are shown in Figure 6 for the visibility amplitudes for the best-fitting models. The models make a wide variety of predictions for future baselines, and the black hole shadow appears as a local minimum in the visibility amplitude near $3000M\lambda$ in the 515h and 715h models.

In addition to visibility amplitudes, phases also carry impor-

tant information about the image structure. The closure phase is formed by summing phases over a triangle of baselines, and is more robust to instrumental errors than individual phase measurements. For favored (and most) position angles for all best-fitting models, the closure phase is near zero, in agreement with recent mm-VLBI observations (Fish et al. 2011). In addition, the black hole shadow shows up as a highly variable closure phase either vs. position angle or time for position angles where the shadow is accessible. For nearly co-linear baselines such as those including current mm-VLBI telescopes, the closure phase tends to be near zero except for viewing orientations corresponding to the black hole shadow. However, phase information is more interesting for other baseline triangles. Depending on viewing orientation and model, a wide range of possible closure phases are possible, many of which differ significantly from zero. Measuring closure phase in future mm-VLBI campaigns will therefore provide significant additional constraints on the models.

At 0.87mm (Figure 7), the other potential wavelength for future mm-VLBI observations, the effects of interstellar scattering are greatly reduced. These images have intrinsically steeper emissivities, however, so that the emission is more concentrated and the black hole shadow is less apparent. For these reasons, shorter wavelengths may be better suited for constraining parameters and testing accretion models than for detecting the black hole shadow. The structure and total flux of the accretion flow at this wavelength are poorly constrained, and the different simulations predict a wide range of both possible image structures and fluxes. For this reason, 0.87mm VLBI may be better for constraining the models. Even a simultaneous spectral constraint at 0.87mm along with 1.3mm could distinguish between many of the possibilities.

6.1.1 Implications for mm-VLBI observations

While a crescent morphology is often found for mm tilted disc images of Sgr A* (especially at 1.3mm), similar to previous models of untilted discs, their time-dependent structures are completely different. Untilted disc images are basically static, as shown in the bottom row of Figure 8. Four images from the 90h simulation are shown spanning the simulation duration ($\simeq 25$ hours for Sgr A*). Even as the flux varies by $\simeq 50$ per cent, the image structure remains virtually unchanged. Tilted disc images, on the other hand, can undergo major structural changes even on relatively short timescales (hours, top row of Figure 8). Thus far, no significant structural changes have been detected with mm-VLBI, consistent with the untilted models. With better coverage, higher sensitivity, and more epochs of data, time variations in structure will become a powerful means to distinguish between untilted and tilted accretion disc models.

Lense-Thirring precession (§2) is another source of possible inter-epoch variability for tilted disc models of Sgr A*. The image structure depends strongly on the observer azimuth (Figure 9), which would effectively change as the disc precesses. Future mm-VLBI observations could then find evidence for this general relativistic effect in the Galactic centre. Unfortunately, the relevant timescale is highly uncertain. It depends sensitively on the effective “outer” radius of the accretion flow, its radial density profile, and the black hole spin. The outer radius is especially problematic, since both its location and interpretation are uncertain for the col-

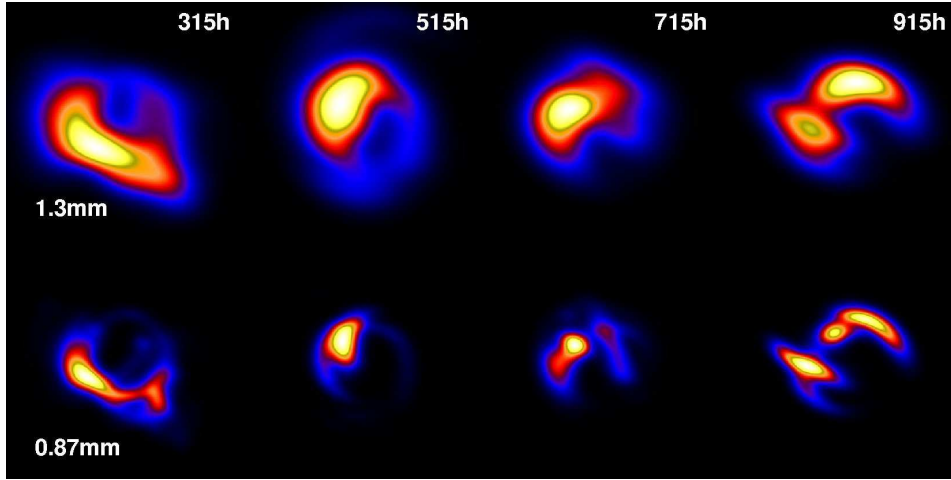


Figure 7. Scatter-broadened best-fitting images at 1.3mm (top) and 0.87mm (bottom). The scaling is the same as in Figure 1. At 0.87mm, the images are easier to distinguish and the black hole shadow is less prominent.

tionless plasma around Sgr A*. In terms of these parameters, the precession time is given by (Fragile et al. 2007):

$$t_{\text{prec}} \simeq \frac{1.3}{a} \left(\frac{r_{\text{out}}}{1000M} \right)^2 \text{yr}, \quad (2)$$

where r_{out} is the effective outer radius. We have assumed $\rho \propto r^{-3/2}$ as expected for Bondi accretion and as found by hydrodynamical simulations of large-scale accretion onto Sgr A* (Cuadra et al. 2006). The precession time is shown in Figure 10 as a function of outer radius for both the Bondi and RIAF solutions. In both cases, for large ranges of outer radius, the precession timescale is likely to be longer than the length of individual mm-VLBI campaigns (days, shaded gray region in Figure 10) but shorter than the length of the entire Event Horizon Telescope experiment (years). This is the case, for example, for both density profiles if the effective outer radius corresponds to the circularization radius found for the accretion flow by Cuadra et al. (2006) (orange shaded region in Figure 10). Alternatively, if the outer radius is extremely small ($r_{\text{max}} \lesssim 100M$), as Pang et al. (2011) found using MHD simulations with a strong large-scale magnetic field, then it could be possible for individual mm-VLBI epochs to span a precession time.

Current data are insufficient to meaningfully test for changes in observer azimuth (and precession) between or within epochs. The prospects for detecting Lense-Thirring precession with Event Horizon Telescope observations will be considered in more detail in future work.

6.2 Spectra

Spectra from the best-fitting tilted disc models are shown in Figure 11. The black lines show the average over observer time, while the dark gray envelope indicates the range. These models cannot explain the radio emission outside the sub-mm bump due to their limited spatial extent and lack of non-thermal emission. The IR tilted disc spectra, however, are much different than any from previous MHD simulations. With purely thermal electrons and no additional free parameters, all best-fitting models to the mm data are consistent with upper limits in the far- and mid-IR while producing the observed flux range in the near-IR (NIR) (although

the 915h model marginally violates the mid-IR upper limit from Schödel et al. 2011).

The mean spectra from the 515h, 715h, and 915h models are in remarkable agreement with reported mean values from Schödel et al. (2011) and the median value from Dodds-Eden et al. (2011). Further, the NIR spectral indices (defined as $F_\nu \propto \nu^{-\alpha_{\text{NIR}}}$ and listed in Table 3) from these models are within the range reported for Sgr A* (Ghez et al. 2005; Gillessen et al. 2006; Hornstein et al. 2007). The spectral index from the 515h model is in remarkable agreement with the result found by Hornstein et al. (2007), while those from the 715h and 915h models agree with the redder reported spectral index of Gillessen et al. (2006). The 315h spectrum underproduces the average NIR emission and its spectral index is steeper than observed. Other model spectra from these simulations may provide excellent fits to the observed NIR emission in Sgr A* as well, and the NIR data could be included in the joint fitting in future studies.

Spectra from untilted disc simulations have similar shapes to that shown for 90h in the left panel of Figure 12 (e.g., Mościbrodzka et al. 2009). The NIR emission is on the exponential tail of the synchrotron spectrum. For this reason, the untilted models underproduce the observed emission by several orders of magnitude and have much redder spectral indices than observed. Comparing the 90h spectrum with that from 515h (right panel of Figure 12) shows that distinct electron populations (and/or a non-thermal distribution function) are crucial for simultaneously producing the mm to NIR spectrum.

The NIR emission in the tilted models is produced by extremely hot electrons ($T_e \approx 1 - 4 \times 10^{12}$ K) near the black hole ($r \approx 3M$). Heating from the standing shocks in the tilted disc models allow for multiple electron populations, some of which can be at very high temperatures. These can effectively mimic a power law tail to the synchrotron emission, especially since they are at significantly lower particle densities than the electrons producing the mm bump (§6.4). This physical heating mimics the effect of adding a non-thermal tail to the electron distribution function (e.g., Yuan, Quataert & Narayan 2003).

These hot electrons are also the reason we discard models with $T_i/T_e \gtrsim 3$ for the 515h and 715h simulations, despite the fact that some of them can fit the mm-VLBI and spectral observations.

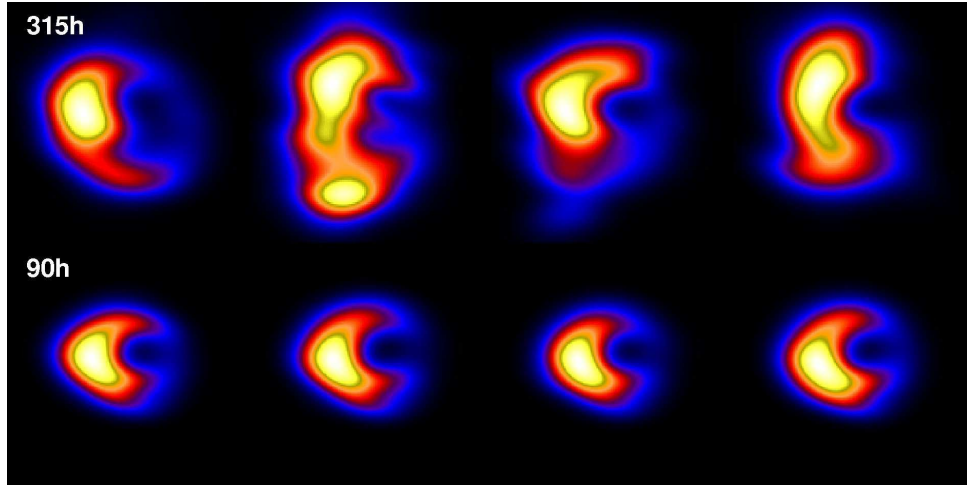


Figure 8. Images at four observer times for the 315h (top row) and 90h (bottom row) simulations including the effects of interstellar scattering. The scaling is the same as in Figure 1. The structure of images from untilted models such as 90h show very little time variability, while those from tilted models can change significantly on hour timescales.

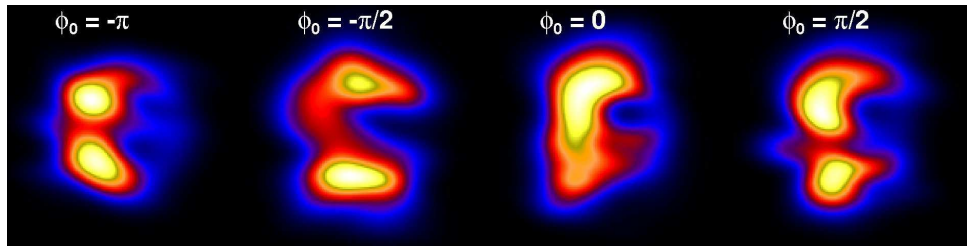


Figure 9. Images at four observer azimuths for the 315h simulation including the effects of interstellar scattering. The scaling is the same as in Figure 1. The image structure changes significantly with observer azimuth, and these changes will be observable on the precession timescale.

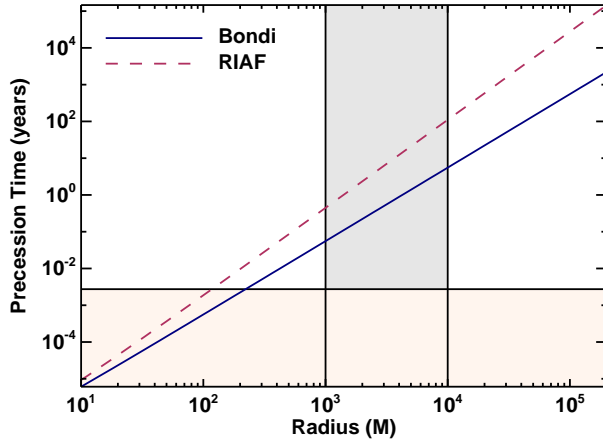


Figure 10. Precession time as a function of outer accretion flow radius ranging from the event horizon to the Bondi radius for radial power law surface density profiles corresponding to RIAF and spherical (Bondi) accretion models. If the effective outer accretion flow radius is $\lesssim 10^{3-4} M$ (gray shaded region, Cuadra et al. 2006), then precession should occur on year timescales, potentially observable as changes between epochs of mm-VLBI observations. Only for extremely small outer radii would significant precession occur within a single epoch of observations (day timescales, yellow shaded region).

Table 3. NIR Variability Parameters

	α_{NIR}	$\exp \mu$ (mJy)	σ
315h	-4.1 ± 1.0	$(0.7 - 1.9) \times 10^{-2}$	11 – 18
515h	-0.5 ± 0.1	1.1 – 1.3	1.8 – 2.0
715h	-1.6 ± 0.7	0.5 – 0.7	3.0 – 3.4
915h	-2.2 ± 0.4	1.0 – 1.3	1.6 – 1.7

Larger accretion rates are required to match the observed mm flux for larger T_i/T_e . The peak synchrotron frequency scales as,

$$\nu_c \sim BT_e^2 \sim \sqrt{MT_e^2}, \quad (3)$$

while the peak flux scales roughly as

$$F_{\nu_c} \sim nB^2T_e^2 \sim \dot{M}^2T_e^2, \quad (4)$$

so that ν_c decreases for larger T_i/T_e at fixed flux. This scaling causes the high frequency parts of the spectra to shift up in normalization and down in frequency. The approximately power law tail can extend into the optical/UV when $T_i/T_e = 1$, and increasing its normalization leads to the violation of many IR upper limits. Although we do not include IR data in the fitting, we do discard models which violate many IR upper limits.

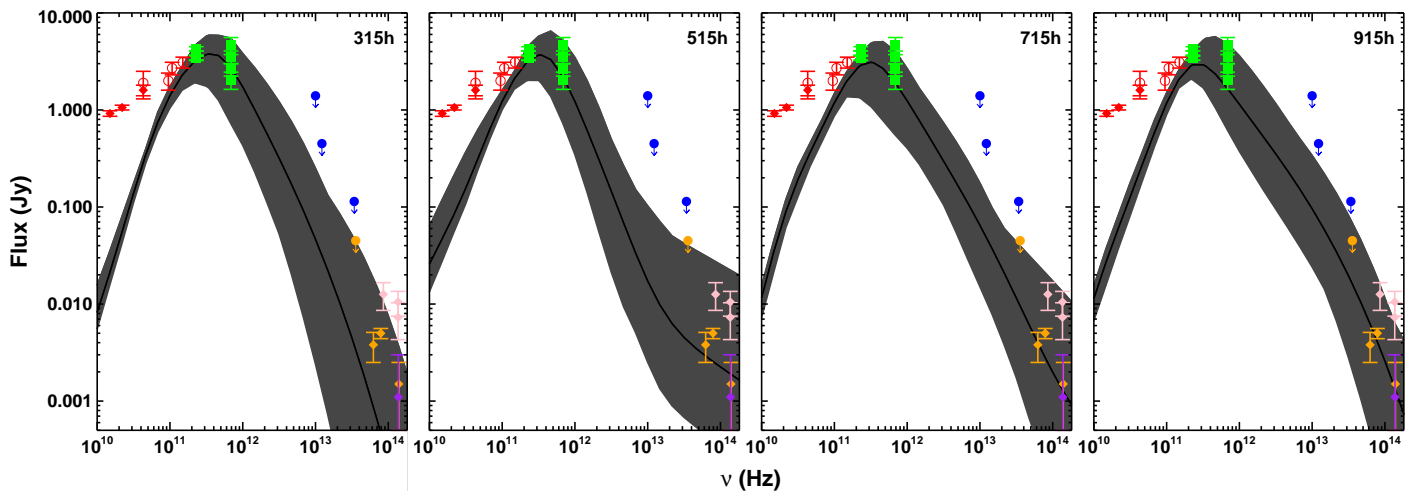


Figure 11. Best-fitting model spectra compared to Sgr A* data. The solid curves are the median values at each frequency over observer time, while the dark gray envelope shows the range. Radio data are from Falcke et al. (1998, open circles) and An et al. (2005, filled diamonds). The models are fit to the mm data (filled squares, Marrone 2006), but are in good agreement with the mean/median (orange and purple, Schödel et al. 2011; Dodds-Eden et al. 2011, respectively) and flaring (pink, Genzel et al. 2003) NIR data with no additional free parameters. They also satisfy observational upper limits in the mid-IR (blue upper limits, Melia & Falcke 2001, and references therein). At lower frequencies the non-thermal emission is produced outside of the simulation domain, either in the accretion flow (Yuan, Quataert & Narayan 2003) or in a short jet (Falcke & Markoff 2000).

6.3 Millimetre to infrared variability

Radiative models of Sgr A* based on simulations are thus far the only to self-consistently include variability information (Goldston, Quataert & Igumenshchev 2005; Dexter, Agol & Fragile 2009; Dexter et al. 2010; Dolence et al. 2012). Best-fitting models to mm-VLBI and spectral information from untilted GRMHD simulations naturally produce millimeter variability qualitatively consistent with that observed (Dexter, Agol & Fragile 2009; Dexter et al. 2010). This variability is due to relatively global ($m = 0, 1$) fluctuations in the particle density and magnetic field strength, and is strongly correlated with the accretion rate. We find similar mm light curves for the best-fitting tilted disc models, as shown in Figure 13. All of the best-fitting light curves exhibit variability on hour timescales with $\lesssim 50$ per cent amplitudes, roughly in agreement with observations. Millimeter “flares” would be identified as two per light curve, consistent with their observed frequency in Sgr A*. However, tilted disc models produce larger amplitude and longer duration flares than their untilted counterparts (cf. Figure 6 of Dexter et al. 2010). The variability is still strongly correlated with the accretion rate, which also varies more in tilted disc simulations.

As discussed above, tilted disc models naturally produce roughly the correct mean levels of IR emission, very different from previous numerical accretion flow models based solely on thermal electrons (e.g., Goldston, Quataert & Igumenshchev 2005; Mościbrodzka et al. 2009). The H ($1.6\mu\text{m}$), K ($2.2\mu\text{m}$), and L ($3.6\mu\text{m}$) band light curves from the best-fitting models to the mm data are shown in Figure 14. In all cases, the NIR emission is highly variable, with factor of $\simeq 5 - 20$ increases over the mean level on $\lesssim 1$ hr timescales, consistent with observations. The time sampling in the light curves is 1 – 10 minutes, depending on the simulation. The 915h simulation, with 1 minute sampling, easily resolves the NIR flux variations. The shortest significant flux variations (factors of $\gtrsim 2$) occur on timescales $\simeq 5 - 15$ minutes. Substructure in the 315h and 715h light curves, with 10 minute sampling, is only marginally resolved.

The various models differ substantially in the predicted NIR spectral slope (see § and Table 3). Similarly, two of the spectral slopes are time variable (315h and 715h), while the others are nearly constant (515h and 915h). The flux distributions of all of the light curves are fairly well described by a log-normal:

$$P(F_\nu; \mu, \sigma) = \frac{1}{\sqrt{2\pi}\sigma F_\nu} \exp\left(-\frac{(\ln F_\nu - \mu)^2}{2\sigma^2}\right), \quad (5)$$

with parameters μ and σ . The median is $\exp(\mu)$, and σ represents a multiplicative standard deviation. This model provides a better description than a standard Gaussian, as Dodds-Eden et al. (2011) found for Sgr A* data. The parameters inferred from our K-band light curves are given in Table 3. The ranges represent the results of fitting with various bin sizes.

Power spectra from all the tilted disc models are qualitatively similar to that for 915h (thick solid curve in Figure 15). The slope is fairly shallow (slope $\simeq -1$) on timescales significantly longer than that of the marginally stable orbit ($\gtrsim 10$ min), although the effective inner disc edge is well outside of this location (Fragile 2009; Dexter & Fragile 2011). On shorter timescales the power spectrum steepens to a slope $\simeq -4.5$. Fit with a single power law, the slope is $\simeq -2.3$, consistent with observations (Meyer et al. 2008; Do et al. 2009).

Dolence et al. (2012) found a broken power law power spectrum in a model of Sgr A* from an untilted GRMHD simulation with a similar break frequency. However, we find no significant quasi-periodic oscillations similar to what they reported near the frequency of the marginally stable orbit. Using many cameras spaced in observer azimuth, they decomposed the power spectrum into azimuthal modes (their Eq. 1 and Fig. 1). A comparison is shown in Figure 15. Unlike in their models, the $m = 0$ mode is dominant, with $m = 1, 2$ only contributing on the shortest timescales. These discrepancies could be due to differences in the simulations (either numerical algorithms or duration), or due to physical differences between tilted and untilted accretion discs.

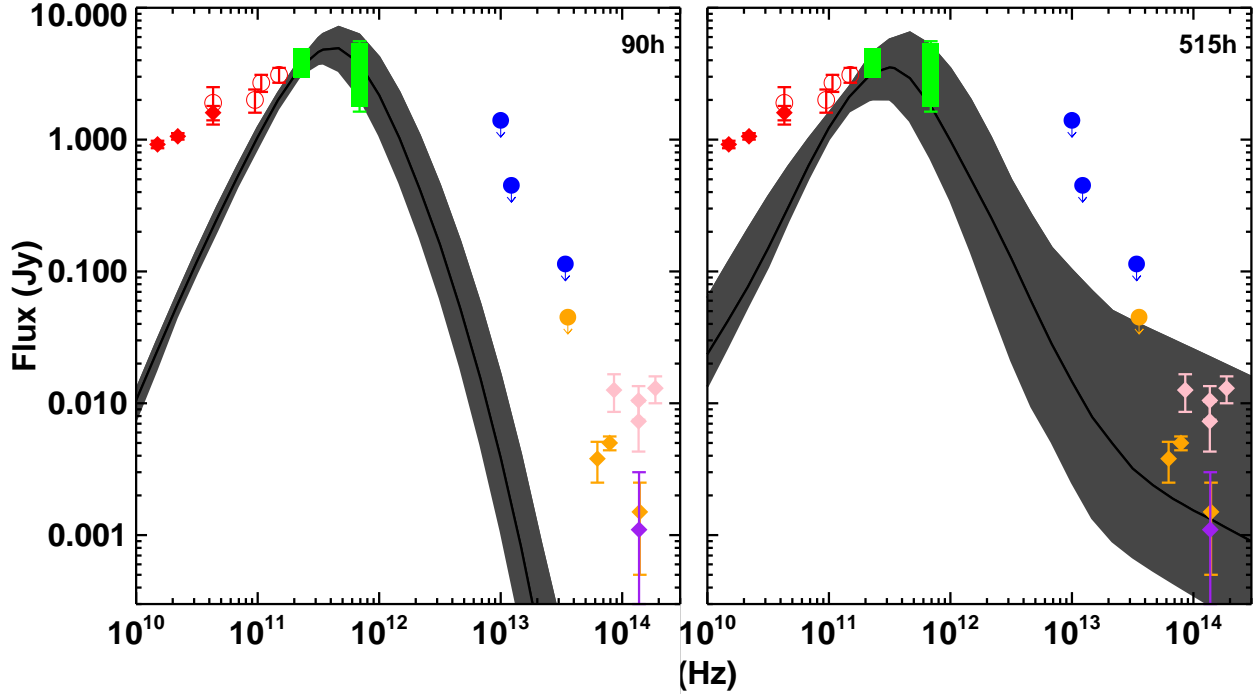


Figure 12. Spectra from best-fitting untilted (90h, left) and tilted (515h, right) simulations. Sgr A* data are the same as in Figure 11. In both cases the spectra are fit to the green sub-mm points. Multiple electron populations from shock heating in tilted discs can naturally produce the observed NIR emission, which is underproduced by ≈ 2 orders of magnitude in untilted simulations. Other untilted simulations exhibit larger amplitude variability than 90h, but its spectral shape is representative.

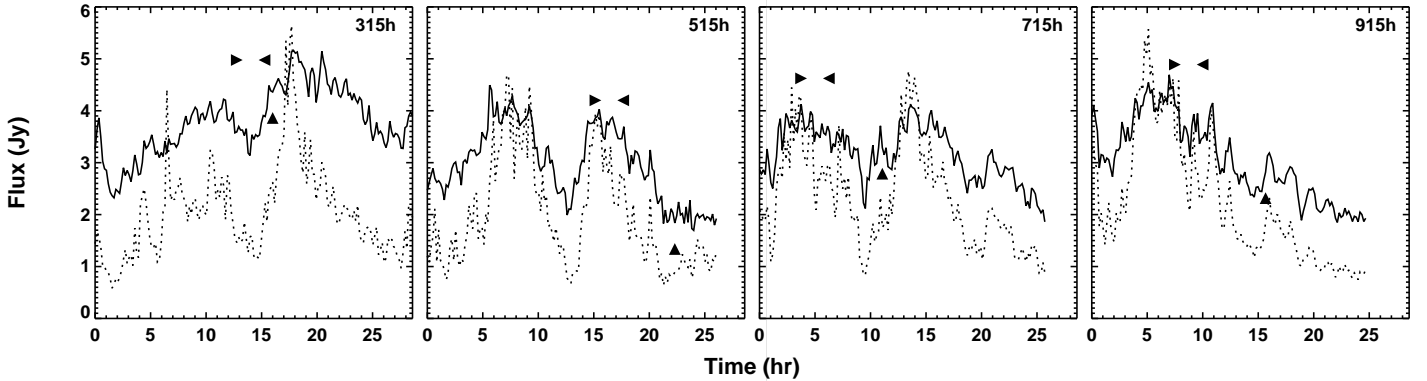


Figure 13. Light curves from the best-fitting models at 1.3mm (230 GHz, solid lines) and 0.4mm (690 GHz, dotted lines). The times of best fit to the visibility data are shown as upward triangles, while the ranges of times averaged for the best fit to the spectral data are bracketed by left and right facing arrows. The simulated light curves exhibit 50 per cent variability on hour timescales, similar to the untilted case and in qualitative agreement with observations. The mm spectral index increases with flux, because the optical depth is lower at higher frequency.

6.4 Physical origin of time-variable mm and NIR emission

The mm emission in the tilted disc models arises from hot, dense electrons in the inner radii of the simulations. Typical parameters of mm electrons are similar to those in untilted discs: $n \sim 10^7 \text{ cm}^{-3}$, $B \sim 50 \text{ G}$, $T_e \sim 6 \times 10^{10} \text{ K}$. As discussed above, this tends to be where densities and field strengths are highest: either in the post-shock fluid or in the midplane of the inner radii of the tilted accretion flow. Due to the asymmetry in the shocks and subsequent infall, the emission geometry is different from untilted simulations. The mm variability in the tilted disc models is, however, essentially the same as in untilted models. The variability is caused by

relatively global fluctuations in the particle density and magnetic field strength. Most of the power in these fluid variables as well as in the emissivity is in the $m = 0$ mode, although there is also significant power in $m = 1, 2$, particularly in the form of spiral waves. The 0.4mm (690 GHz) light curve is strongly correlated with the accretion rate through the inner boundary, suggesting that at least the $m = 0$ power is from global changes in the accretion rate. The global nature of the variability may explain its similarities in tilted and untilted models, despite significant differences in their dynamics.

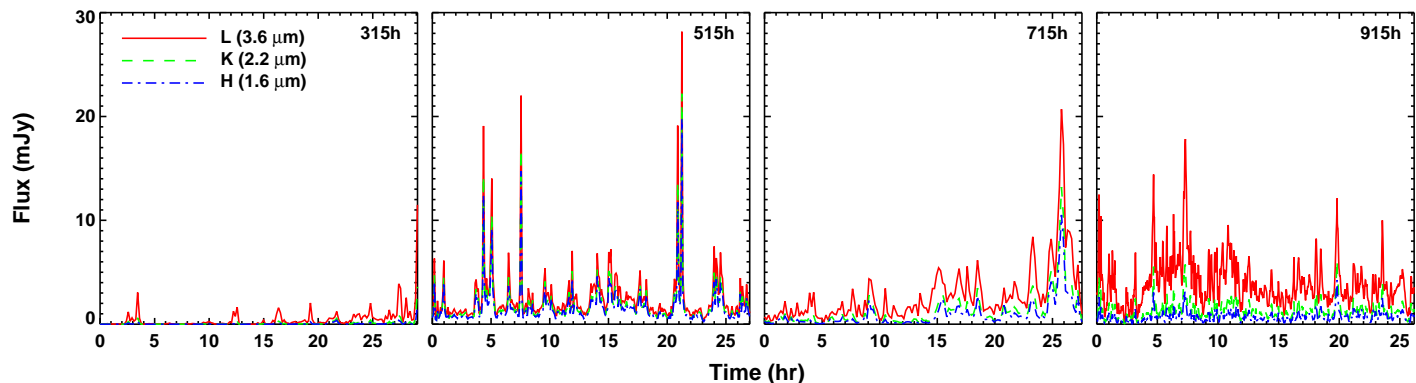


Figure 14. Near-infrared light curves from the best-fitting models in the H, K, and L bands. All of the simulated NIR light curves are highly variable on short (\lesssim hr) timescales. The 315h simulation underproduces the observed NIR flux and its variability. The 515h, 715h, and 915h models produce the observed flux range and exhibit “flares” with roughly the right amplitudes (factors \lesssim 30) and timescales (\simeq 1hr). The 315h and 715h spectral slopes are time-variable, while those from the 515h and 915h models are nearly constant with NIR flux.

Dexter et al. (2010) found that a simple approximate emissivity, $j_\nu \propto nB^2$, captured the shape of the mm light curves from untilted simulations of Sgr A*. This is the expected form for isothermal synchrotron emission with $T_e \simeq 6 \times 10^{10}$ K, and demonstrates that temperature fluctuations are not important for driving the variability. We find the same result for the tilted disc models. This variability mechanism is not magnetic reconnection, since the tilted simulations do not capture heat lost by grid-scale magnetic dissipation. It is also not orbiting hot spots, as the $m = 0$ power dominates the fluctuations.

The NIR emission in the models is entirely optically thin, and dominated by very small regions at small radius ($r \simeq 3M$) in the simulation with lower densities ($n \sim 10^5 \text{ cm}^{-3}$), similar magnetic field strengths ($B \sim 50$ G), and hot temperatures ($T_e \gtrsim 10^{12}$ K). This location is fairly insensitive to spin, and is inside the marginally stable orbit for all but the 915h simulation. These are lower particle densities and higher electron temperatures than previously reported for IR-emitting electrons from axisymmetric, untilted GRMHD simulations (Mościbrodzka et al. 2009). In their simulations, the NIR emission was dominated by heating from numerical magnetic reconnection in current sheets, which is thought to be an artifact of axisymmetry. In our model, the NIR-emitting electrons are heated by the non-axisymmetric standing shocks. This is the only source of entropy generation in these simulations, since heat from numerical reconnection is lost from the grid. For example, the maximum temperature obtained anywhere in the 90h simulation is $\lesssim 10^{12}$ K.

The NIR “flares” in our models are due to fluctuations in the particle density, field strength, and electron temperature of these hot post-shock electrons. The 915h K-band light curve can be recovered approximately with an emissivity $j_\nu \propto nB^2$, as long as only hot electrons are included ($T_e > 5 \times 10^{11}$ K). In the 515h and 715h simulations (with hotter electrons), the emissivity can be approximated as $j_\nu \propto nBT_e$. Temperature fluctuations are important in the 515h and 715h simulations, but not in 915h. The approximate forms can be understood by the variations in emissivity expected from fluctuations in the individual quantities at the appropriate ratio of ν/ν_c . This ratio is near 1 for the hotter 515h and 715h simulations, and $\approx 10 - 20$ for 915h. Closer to $\nu = \nu_c$, the emissivity is less strongly dependent on B and T_e .

General relativistic effects are also important for the NIR light curves from 515h and 715h. Many of the flares in these models correspond to extreme gravitational lensing events, where emission

from hot electrons behind the black hole is lensed into a bright ring. An example from the 515h model is shown in Figure 16. A flare occurs between the first and second panels when hot gas behind the black hole is strongly lensed, concentrating its emission in a bright ring at the circular photon orbit. In the subsequent frames, this hot material passes by the black hole and moves to larger radius, leading to a decay of the flare. The lensing acts as a filter, enhancing the emission from electrons at larger radius ($r \gtrsim 3M$), and can produce modulations in the light curves of order the observed flux.

The NIR image structure is highly variable, and so is its centroid. The K-band centroid position is shown in Figure 17. The typical excursions are $\simeq 30 - 50 \mu\text{as}$ in all best-fitting models except that from the 915h simulation. The position wander is only weakly correlated with the NIR flux. All periods of rapid variability and very high NIR fluxes also exhibit significant centroid motions, but not all periods of large position wander correspond to NIR flares.

The NIR spectral index is set by the critical frequency for synchrotron emission,

$$\nu_c = 6 \times 10^{12} \left(\frac{T_e}{10^{12} \text{ K}} \right)^2 \left(\frac{B}{50 \text{ G}} \right)^{1/2} \text{ Hz.} \quad (6)$$

This primarily depends on electron temperature, which varies between simulations. The NIR electrons are coldest in the 315h simulation, and hottest in the 515h simulation. Somewhat surprisingly, the shock heating is less effective in the 715h and 915h simulations. Dexter & Fragile (2011) argued that the non-axisymmetric standing shocks are stronger in higher spin simulations. Colder NIR electrons and lower critical frequencies lead to more negative spectral indices. These also tend to be more variable, since the emissivity depends strongly on frequency when $\nu/\nu_c \gg 1$. When $\nu/\nu_c \simeq 1$, as for the 515h simulation, the emissivity is fairly flat, and the spectral index is nearly constant.

The mm and NIR light curves are uncorrelated in this model, since they arise from different populations of electrons. The full 690 GHz and K-band light curves and their cross-correlation are shown in Figure 18. Although the full duration light curves are uncorrelated, 6 hour segments can produce spurious peaks in the cross-correlation with hour lags, similar to those reported for Sgr A* (e.g., Yusef-Zadeh et al. 2008).

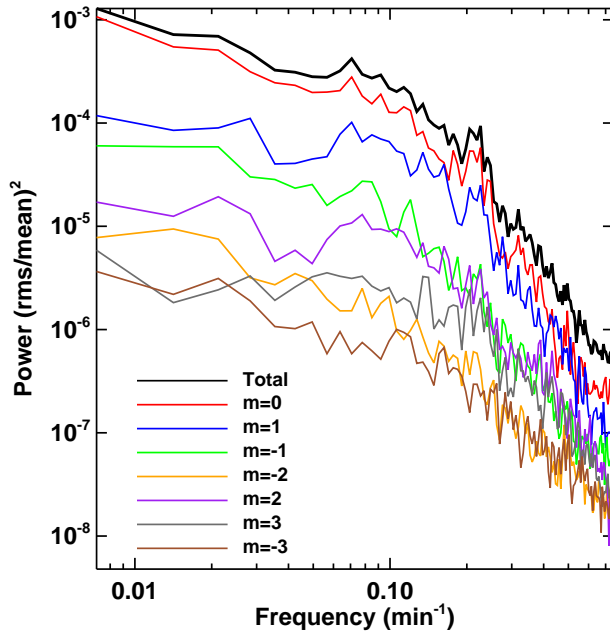


Figure 15. NIR K-band ($2.2\mu\text{m}$) power spectrum (thick solid curve) from the best-fitting 915h model, averaged over 10 evenly-spaced light curve segments. The power spectrum is further decomposed in azimuthal mode segments, as done in Dolence et al. (2012). Both the overall power spectrum and those from individual azimuthal modes are well described by broken power laws with break frequencies $\sim 10\text{min}^{-1}$. The full power spectrum has slopes $\simeq -1$ and -4.5 .

7 DISCUSSION

Geometrically thick, low luminosity accretion flows do not align with their central black holes. The current source of accretion onto Sgr A* is winds from massive stars, whose net angular momentum is almost certainly unrelated to the spin axis of the black hole. Both the current accretion rates onto Sgr A* at the Bondi radius and in the inner radii are orders of magnitude smaller than required for sufficient mass accretion to have changed the black hole spin orientation over a Hubble time. Therefore, it is highly unlikely that the black hole spin axis in Sgr A* aligns with the angular momentum of the accreting gas. We have constructed the first radiative models of Sgr A* from misaligned (tilted) black hole accretion flows by performing radiative transfer calculations on data from GRMHD simulations (Table 1). These models provide an excellent description of existing observations, and are significantly different from any theoretical model previously considered. Even for the modest 15° misalignment considered between black hole spin and accretion angular momentum axes, the (thermo)dynamics of the accretion flow change drastically. Non-axisymmetric shocks from the convergence of eccentric orbits in the warped disc give rise to asymmetric image morphologies, leading to the breakdown of many simplifying assumptions in the untilted models. The observer azimuthal viewing angle becomes an important new parameter, and the dependence of observables on both the viewing geometry and the ion-electron temperature ratio become non-trivial. The combination of these factors greatly expands the possible parameter space for tilted disc models relative to those assumed in all previous models of Sgr A*.

There are numerous implications. The parameters of both

the black hole and the viewing geometry are poorly constrained (Figures 2 and 3) by mm-VLBI and spectral observations. Previously reported parameter constraints (Broderick et al. 2009, 2011; Mościbrodzka et al. 2009; Dexter, Agol & Fragile 2009; Dexter et al. 2010; Shcherbakov, Penna & McKinney 2010) only apply if the black hole spin or tilt values are extremely small. Upper limits from this work are $a < 0.3$ or $\beta < 15^\circ$, although qualitatively similar behavior has been seen in a simulation with $\beta = 10^\circ$ (Henisey et al. 2009). The best-fitting models (Table 2) to the mm data sort into two groups at low ($10^{-9} - 10^{-8} M_\odot \text{yr}^{-1}$) and high ($\gtrsim 10^{-7} M_\odot \text{yr}^{-1}$) time-averaged mass accretion rates.

The “crescent” black hole images reported by Dexter et al. (2010) are also found from these best-fitting tilted images at 1.3mm, especially when including the effects of interstellar scattering. For this reason, the black hole shadow is still expected to be accessible, although huge uncertainties in the viewing geometry for these models prevent a robust prediction for baselines where it should be seen. In two of the best-fitting models (see Figure 6), the shadow is visible on baselines between telescopes in Chile (ALMA/APEX) and Mexico (LMT), but a wide variety of other geometries are nearly as likely. The mm variability properties reported previously (Dexter, Agol & Fragile 2009; Dexter et al. 2010) qualitatively hold for the tilted disc models, although their variability amplitudes and characteristic timescales seem somewhat larger (Figure 13).

Although images from tilted discs are crescents at 1.3mm, at 0.87mm the images can become double-peaked due to emission from near the standing shocks (915h model in Figure 7). The structure of the tilted images is also highly time-variable, in stark contrast to the static morphology in the untilted case (Figure 8). Tilted and untilted models can then be distinguished either with higher frequency mm-VLBI or simply with many epochs of observations using the current array. Polarized mm-VLBI observations may also help to distinguish between models. Shcherbakov, Penna & McKinney (2010) found that spectropolarimetric data contain comparable constraining power as current mm-VLBI observations.

Perhaps the most important difference is that the low accretion rate best-fitting models (those from the 515h, 715h, and 915h simulations) naturally reproduce IR spectral (Figure 11) and variability (Figure 14) properties consistent with observations, while those at high mass accretion rates (from the 315h simulation) underproduce the observed flux. All models satisfy the observed upper limits on mid-infrared emission (Telesco, Davidson & Werner 1996; Cotera et al. 1999; Schödel et al. 2011). All three low accretion rate models are in excellent agreement with the reported mean NIR fluxes from Sgr A* (Schödel et al. 2011; Dodds-Eden et al. 2011). Flux distributions from the 515h and 915h models are well described by a log-normal, and the inferred parameters (Table 3) are in excellent agreement with those found by Dodds-Eden et al. (2011). Both the mean and time-dependence of the NIR spectral index varies considerably between models. The 515h spectral index is constant in time with a value of $\alpha_{\text{NIR}} = -0.5 \pm 0.1$, nearly identical to the observations of Ghez et al. (2005) and Hornstein et al. (2007). The 715h and 915h light curves have much redder spectral indices, and the 715h spectral index increases with flux. These values are in good agreement with Gillessen et al. (2006). Because of the short duration of our light curves ($\simeq 25\text{hr}$), it is unclear whether the 515h, 715h, and 915h light curves are best interpreted as different states of the same theoretical model, or as a means to distinguish between the models.

In any event, this is the first model of Sgr A* that self-

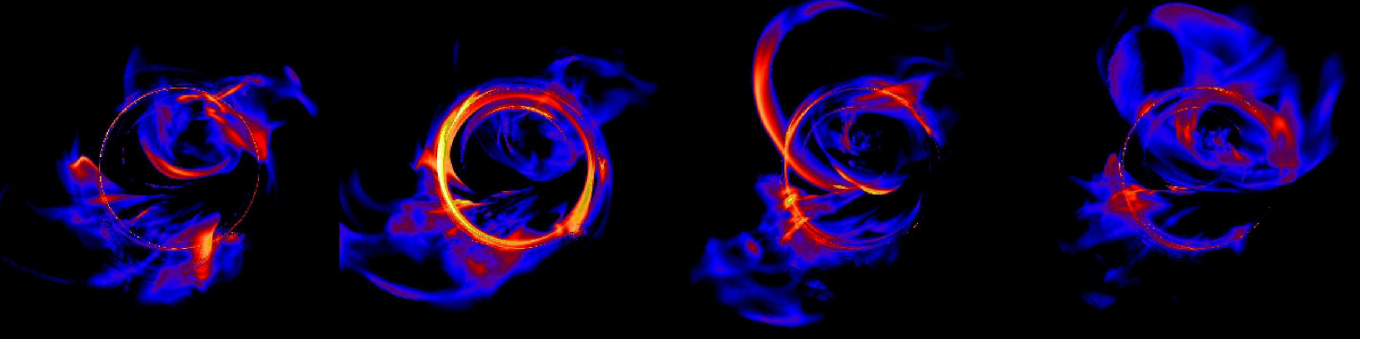


Figure 16. H-band ($1.6\mu\text{m}$) images from the 515h model spaced $\simeq 5\text{min}$ apart during an NIR “flare” with a factor of $\simeq 4$ flux variation between the first and second images. The images are scaled logarithmically with a dynamic range of 2048, and the panel size is $85 \times 85\mu\text{as}$. The flare emission is clearly lensed and concentrated at the photon ring, corresponding to the unstable photon orbit in the Kerr spacetime.

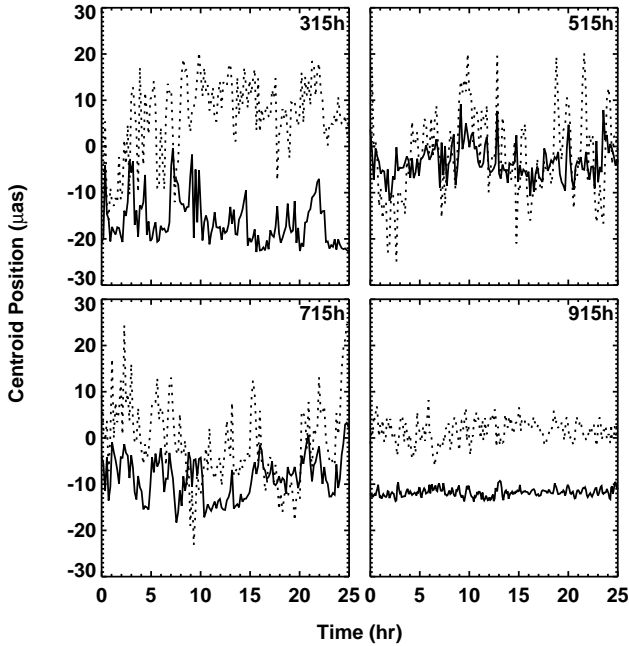


Figure 17. X (solid) and Y (dotted) centroid positions for the K-band ($2.2\mu\text{m}$) images. Periods of rapid centroid movement of $\simeq 30 - 50\mu\text{as}$ occur every few hours in all models but 915h, and should be detectable by the future VLT instrument GRAVITY.

consistently produces the observed time-variable mm to NIR emission. The two are completely uncorrelated. The mm variations are due to magnetic turbulence and are strongly correlated with the accretion rate. The NIR variations are caused by particle density, field strength, and temperature variations in tenuous, hot gas heated by the non-axisymmetric standing shocks, and can be significantly modulated by extreme gravitational lensing. Short segments of these light curves can, however, still lead to the reported weak correlations (Figure 18). We caution therefore that cross-correlation coefficients of $\lesssim 0.6$ between wavebands in single epoch observations do not necessarily imply a common physical origin.

This NIR emission model is completely novel. It is not due to orbiting or expanding “hotspots” (Broderick & Loeb 2005; Eckart et al. 2006; Yusef-Zadeh et al. 2008; Eckart et al. 2012). However, significant structural changes can still be seen during large changes in NIR flux (Figure 17). It is similar in spirit to models that invoke magnetic reconnection events (Dodds-Eden et al.

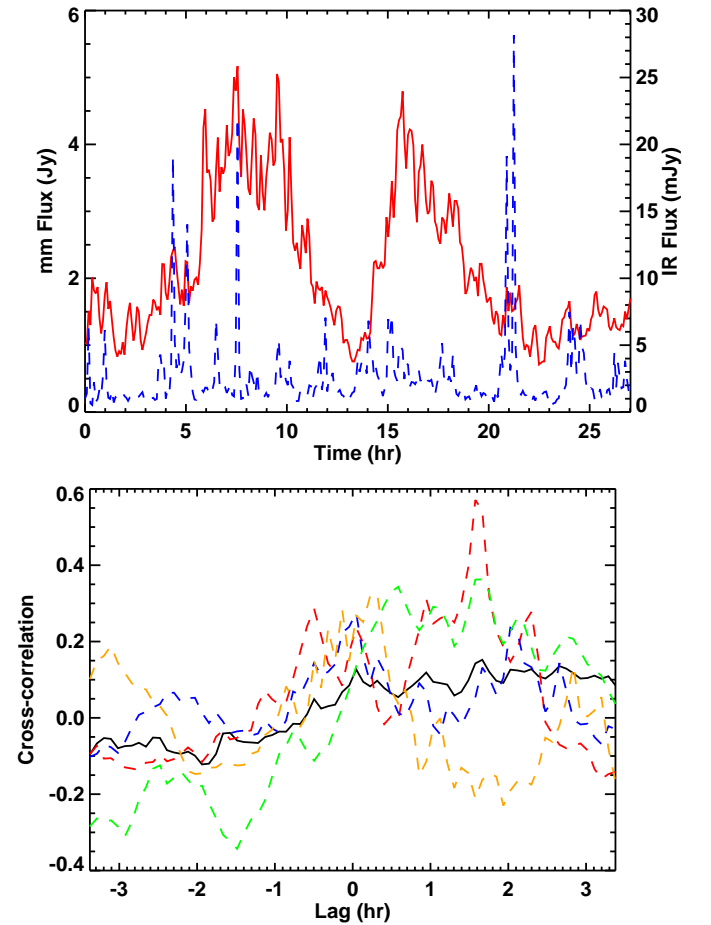


Figure 18. Top: Light curves from the 515h simulation at 0.4mm (red) and $3.6\mu\text{m}$ (blue). Bottom: Cross-correlation of the full light curves (solid curve) and four evenly spaced segments (dashed curves). For these short (several hour) durations, lags can be found at correlations of $\simeq 0.4 - 0.6$ as reported in the literature (e.g., Yusef-Zadeh et al. 2008), despite the fact that the full light curves are uncorrelated.

2010) to accelerate electrons to the observed high energies. But magnetic reconnection cannot heat particles in these simulations. Instead, the heating is from the non-axisymmetric standing shocks in the tilted accretion flow. This emission is also completely dif-

ferent from that described by Dolence et al. (2012), who detected quasi-periodic oscillations in NIR/X-ray light curves of Sgr A* from an untilted GRMHD simulation. Their model underproduces the observed NIR flux by an order of magnitude, similar to previous models from untilted simulations (Dexter et al. 2010). In addition, the NIR/X-ray variability in their model is strongly correlated with that in the mm, in conflict with observations.

These radiative calculations assume that cooling is negligible for the fluid (thermo)dynamics. However, the cooling timescale for the NIR-emitting electrons is short:

$$t_{\text{cool}} \simeq 10 \left(\frac{B}{50G} \right)^{-3/2} \left(\frac{\nu}{10^{14}\text{Hz}} \right)^{-2} \text{min.} \quad (7)$$

At $r \approx 3M$, where the emission is produced, this timescale is still larger than the dynamical time ($t_{\text{dyn}} \simeq 2 \text{ min}$). If this is where the particle heating occurs, ignoring the effects of cooling on the electron temperature may be a safe approximation. We have also assumed a thermal electron distribution function, which is likely incorrect. Both of these limitations can be addressed in future calculations by following particle trajectories through the standing shocks and self-consistently accounting for heating and cooling.

We have only included synchrotron radiation. Including inverse Compton scattering via Monte Carlo calculations (e.g., Dolence et al. 2012) would allow the calculation of X-ray light curves, and in particular the X-ray luminosity during NIR flares. We can crudely estimate this using typical values of fluid variables during rapid changes in NIR flux: $T_e = 2 \times 10^{12}\text{K}$, $R = 1M$ and $n = 10^5\text{cm}^{-3}$ (low, H-band flux of 1 mJy) to $R = 3M$ and $n = 6 \times 10^5\text{cm}^{-3}$ (high, H-band flux of 10 mJy). For this temperature, the Compton peak is at $\sim 1\text{keV}$. The ratios of Compton to synchrotron bolometric luminosities estimated using the formulae in Esin et al. (1996) are $L_C/L_S \simeq 0.1$ (low) and $L_C/L_S \simeq 2$ (high). At those H-band fluxes, the estimated X-ray luminosities are: $L_X \sim 10^{33}\text{erg s}^{-1}$ (low) and $L_X \sim 10^{35}\text{erg s}^{-1}$ (high). These numbers are in rough agreement with observations of X-ray flares (e.g., Baganoff et al. 2001, 2003).

The effects of radiative cooling on multi-wavelength spectra from axisymmetric (aligned) GRMHD simulations have been studied by Dibi et al. (2012, submitted) and Drappeau et al. (2011). They find that adding radiation in post-processing, as done here, is valid for accretion rates $\dot{M} \lesssim 10^{-7} M_{\odot}\text{yr}^{-1}$. All of our best-fitting models satisfy this criterion (Table 2) except for that from 315h, where the accretion rate is slightly larger than this value. Radiative cooling may be important for this and similar models, although it is unknown whether this accretion rate limit applies to tilted discs.

We have only considered four simulations, all with a tilt angle of $\beta = 15^\circ$. The non-conservative GRMHD algorithm used in these simulations leads to a scale height $H/r \simeq 0.1$, whereas the accretion flow onto Sgr A* may have $H/r \simeq 1$. We are unable to probe the dependence of our results on either tilt angle or scale height, both of which may change the formation and strength of the standing shocks. It is unclear whether the models considered here are representative of the range of possibilities from tilted black hole accretion discs.

All of these simulations failed to conserve total energy. We previously found that magnetic energy lost to grid-scale numerical reconnection leads to a radiatively efficient effective luminosity, $\sim 0.1\dot{M}c^2$ (Dexter, Agol & Fragile 2009). Although untilted models based on these simulations give very similar results to those that recapture this energy as heat (Dexter et al. 2010), it is unclear

whether that is the case for tilted discs. The lack of energy conservation means that the only form of entropy generation is through shock heating. Numerical dissipation of magnetic fields would provide another heat source, and could potentially lessen the dramatic effects seen here that are caused by the standing shocks. This issue can be addressed by future energy-conserving tilted simulations.

If standing shocks forming from eccentric orbits in a tilted, warped disc provide the heating mechanism for the observed NIR emission, then the inner disc must be tilted with respect to the black hole spin axis. Then the Galactic centre black hole must have non-zero spin. Furthermore, recent general relativistic, semi-analytic models of geometrically thick tilted accretion discs find that the inner disc aligns with the black hole for $a < 0$ (Zhuravlev & Ivanov 2011). Therefore, if this proposed model for the NIR emission is correct, the black hole in Sgr A* must have positive spin ($a > 0$).

8 SUMMARY

There is no reason to expect alignment between the black hole spin axis and the angular momentum axis of accreting gas in radiatively inefficient sources. We have calculated time-variable mm to NIR emission from the only published numerical models of misaligned (“tilted”) black hole accretion discs and compared them to observations of Sgr A*. Our main results are:

- (i) Tilted disc models provide an excellent description of existing mm-VLBI and spectral observations of Sgr A*.
- (ii) Previously reported parameter constraints from fitting models to mm-VLBI, spectral, and/or polarization measurements are only valid if the spin or tilt value is very small (upper limits of $a < 0.3$, $\beta < 15^\circ$).
- (iii) Predicted images for mm-VLBI are still crescents as in the aligned case, and the black hole shadow, direct evidence for the existence of an event horizon, is still potentially visible on baselines between Mexico and Chile.
- (iv) Heating from non-axisymmetric standing shocks can naturally produce the observed NIR emission. This emission is uncorrelated with the mm variability, which also agrees with observations and is strongly correlated with the mass accretion rate. The X-ray flares in this picture arise from Compton upscattering of NIR seed photons.
- (v) We predict several observational signatures of disc tilt: a) structural changes observable with mm-VLBI from strong asymmetry in the emission region on hour (dynamical) and/or day-year (Lense-Thirring precession) timescales; b) bimodal structures in 345 GHz mm-VLBI images from the presence of standing shocks in the accretion flow; and c) NIR centroid motions of $30 - 50\mu\text{as}$ from extreme gravitational lensing during flares.
- (vi) If the NIR emission is caused by heating from standing shocks in a tilted accretion flow, then the spin parameter of Sgr A* must satisfy $a > 0$.

ACKNOWLEDGEMENTS

JD thanks Eric Agol, Omer Blaes, Josh Dolence, and Eliot Quataert for useful discussions. This work was partially supported by NSF grants AST-0807385 and PHY11-25915, NASA grant 05-ATP05-96, and NASA Earth & Space Science Fellowship NNX08AX59H (JD).

REFERENCES

- Aitken D. K., Greaves J., Chrysostomou A., Jenness T., Holland W., Hough J. H., Pierce-Price D., Richer J., 2000, *ApJ*, 534, L173
- An T., Goss W. M., Zhao J., Hong X. Y., Roy S., Rao A. P., Shen Z., 2005, *ApJ*, 634, L49
- Anninos P., Fragile P. C., Salmonson J. D., 2005, *ApJ*, 635, 723
- Baganoff F. K. et al., 2001, *Nature*, 413, 45
- , 2003, *ApJ*, 591, 891
- Balbus S. A., Hawley J. F., 1991, *ApJ*, 376, 214
- Bardeen J. M., 1973, in *Black holes (Les astres occlus)*, DeWitt B. S., DeWitt C., eds., New York: Gordon and Breach, p. 215
- Bardeen J. M., Petterson J. A., 1975, *ApJ*, 195, L65+
- Bower G. C., Goss W. M., Falcke H., Backer D. C., Lithwick Y., 2006, *ApJ*, 648, L127
- Bower G. C., Wright M. C. H., Falcke H., Backer D. C., 2003, *ApJ*, 588, 331
- Broderick A. E., Fish V. L., Doeleman S. S., Loeb A., 2009, *ApJ*, 697, 45
- , 2011, *ApJ*, 735, 110
- Broderick A. E., Loeb A., 2005, *MNRAS*, 363, 353
- , 2006, *ApJ*, 636, L109
- Chakrabarti S. K., 1985, *ApJ*, 288, 1
- Chan C., Liu S., Fryer C. L., Psaltis D., Özel F., Rockefeller G., Melia F., 2009, *ApJ*, 701, 521
- Cotera A. S., Simpson J. P., Erickson E. F., Colgan S. W. J., Burton M. G., Allen D. A., 1999, *ApJ*, 510, 747
- Cuadra J., Nayakshin S., Springel V., Di Matteo T., 2006, *MNRAS*, 366, 358
- Dexter J., 2011, PhD thesis, University of Washington
- Dexter J., Agol E., 2009, *ApJ*, 696, 1616
- Dexter J., Agol E., Fragile P. C., 2009, *ApJ*, 703, L142
- Dexter J., Agol E., Fragile P. C., McKinney J. C., 2010, *ApJ*, 717, 1092
- Dexter J., Fragile P. C., 2011, *ApJ*, 730, 36
- Do T., Ghez A. M., Morris M. R., Yelda S., Meyer L., Lu J. R., Hornstein S. D., Matthews K., 2009, *ApJ*, 691, 1021
- Dodds-Eden K. et al., 2011, *ApJ*, 728, 37
- Dodds-Eden K., Sharma P., Quataert E., Genzel R., Gillessen S., Eisenhauer F., Porquet D., 2010, *ApJ*, 725, 450
- Doeleman S. S. et al., 2008, *Nature*, 455, 78
- Dolence J. C., Gammie C. F., Shiokawa H., Noble S. C., 2012, *ApJ*, 746, L10
- Drappeau S., Dibi S., Dexter J., Markoff S., Fragile P. C., 2011, in *SF2A-2011: Proceedings of the Annual meeting of the French Society of Astronomy and Astrophysics*, G. Alecian, K. Belkacem, R. Samadi, & D. Valls-Gabaud, ed., pp. 563–565
- Eckart A. et al., 2004, *A&A*, 427, 1
- , 2006, *A&A*, 450, 535
- , 2012, *A&A*, 537, A52
- Esin A. A., Narayan R., Ostriker E., Yi I., 1996, *ApJ*, 465, 312
- Falcke H., Goss W. M., Matsuo H., Teuben P., Zhao J., Zylka R., 1998, *ApJ*, 499, 731
- Falcke H., Markoff S., 2000, *A&A*, 362, 113
- Falcke H., Melia F., Agol E., 2000, *ApJ*, 528, L13
- Fish V. L. et al., 2011, *ApJ*, 727, L36+
- Fragile P. C., 2009, *ApJ*, 706, L246
- Fragile P. C., Anninos P., 2005, *ApJ*, 623, 347
- Fragile P. C., Blaes O. M., 2008, *ApJ*, 687, 757
- Fragile P. C., Blaes O. M., Anninos P., Salmonson J. D., 2007, *ApJ*, 668, 417
- Fragile P. C., Lindner C. C., Anninos P., Salmonson J. D., 2009, *ApJ*, 691, 482
- Genzel R., Schödel R., Ott T., Eckart A., Alexander T., Lacombe F., Rouan D., Aschenbach B., 2003, *Nature*, 425, 934
- Ghez A. M. et al., 2005, *ApJ*, 635, 1087
- , 2004, *ApJ*, 601, L159
- Gillessen S. et al., 2006, *ApJ*, 640, L163
- Goldston J. E., Quataert E., Igumenshchev I. V., 2005, *ApJ*, 621, 785
- Hawley J. F., Guan X., Krolik J. H., 2011, *ApJ*, 738, 84
- Henisey K. B., Blaes O. M., Fragile P. C., Ferreira B. T., 2009, *ApJ*, 706, 705
- Hornstein S. D., Matthews K., Ghez A. M., Lu J. R., Morris M., Becklin E. E., Rafelski M., Baganoff F. K., 2007, *ApJ*, 667, 900
- Huang L., Liu S., Shen Z., Yuan Y., Cai M. J., Li H., Fryer C. L., 2009, *ApJ*, 703, 557
- Ivanov P. B., Illarionov A. F., 1997, *MNRAS*, 285, 394
- Kumar S., Pringle J. E., 1985, *MNRAS*, 213, 435
- Leung P. K., Gammie C. F., Noble S. C., 2011, *ApJ*, 737, 21
- Markoff S., Falcke H., Yuan F., Biermann P. L., 2001, *A&A*, 379, L13
- Marrone D. P., 2006, PhD thesis, AA(Harvard University)
- Marrone D. P. et al., 2008, *ApJ*, 682, 373
- Marrone D. P., Moran J. M., Zhao J.-H., Rao R., 2007, *ApJ*, 654, L57
- McKinney J. C., Blandford R. D., 2009, *MNRAS*, 394, L126
- Melia F., Falcke H., 2001, *ARA&A*, 39, 309
- Meyer L., Do T., Ghez A., Morris M. R., Witzel G., Eckart A., Bélanger G., Schödel R., 2008, *ApJ*, 688, L17
- Mościbrodzka M., Gammie C. F., Dolence J. C., Shiokawa H., Leung P. K., 2009, *ApJ*, 706, 497
- Noble S. C., Leung P. K., Gammie C. F., Book L. G., 2007, *Class. and Quant. Gravity*, 24, 259
- Ohsuga K., Kato Y., Mineshige S., 2005, *ApJ*, 627, 782
- Pang B., Pen U.-L., Matzner C. D., Green S. R., Liebendörfer M., 2011, *MNRAS*, 415, 1228
- Quataert E., 2004, *ApJ*, 613, 322
- Riquelme M. A., Quataert E., Sharma P., Spitkovsky A., 2012, *ArXiv e-prints*
- Schödel R., Morris M. R., Muzic K., Alberdi A., Meyer L., Eckart A., Gezari D. Y., 2011, *A&A*, 532, A83
- Sharma P., Quataert E., Hammett G. W., Stone J. M., 2007, *ApJ*, 667, 714
- Shcherbakov R. V., Penna R. F., McKinney J. C., 2010, *ArXiv e-prints*
- Shiokawa H., Dolence J. C., Gammie C. F., Noble S. C., 2012, *ApJ*, 744, 187
- Telesco C. M., Davidson J. A., Werner M. W., 1996, *ApJ*, 456, 541
- Yuan F., Quataert E., Narayan R., 2003, *ApJ*, 598, 301
- Yusef-Zadeh F. et al., 2006, *ApJ*, 644, 198
- , 2009, *ApJ*, 706, 348
- Yusef-Zadeh F., Wardle M., Heinke C., Dowell C. D., Roberts D., Baganoff F. K., Cotton W., 2008, *ApJ*, 682, 361
- Zhao J.-H., Young K. H., Herrnstein R. M., Ho P. T. P., Tsutsumi T., Lo K. Y., Goss W. M., Bower G. C., 2003, *ApJ*, 586, L29
- Zhuravlev V. V., Ivanov P. B., 2011, *MNRAS*, 415, 2122